KIF5B-ALK, a Novel Fusion Oncokinase Identified by an Immunohistochemistry-based Diagnostic System for ALK-positive Lung Cancer

Kengo Takeuchi,[1] Young Lim Choi,[3] Yuki Togashi,[1] Manabu Soda,[3] Satoko Hatano,[1] Kentaro Inamura,[1] Shuji Takada,[3] Toshihide Ueno,[3] Yoshihiro Yamashita,[3] Yukitoshi Satoh,[2] Sakae Okumura,[2] Ken Nakagawa,[2] Yuichi Ishikawa,[1] and Hiroyuki Mano[3,4]

Abstract

Purpose: EML4-ALK is a transforming fusion tyrosine kinase, several isoforms of which have been identified in lung cancer. Immunohistochemical detection of EML4-ALK has proved difficult, however, likely as a result of low transcriptional activity conferred by the promoter-enhancer region of *EML4*. The sensitivity of EML4-ALK detection by immunohistochemistry should be increased adequately.

Experimental Design: We developed an intercalated antibody-enhanced polymer (iAEP) method that incorporates an intercalating antibody between the primary antibody to ALK and the dextran polymer-based detection reagents.

Results: Our iAEP method discriminated between tumors positive or negative for *EML4-ALK* in a test set of specimens. Four tumors were also found to be positive for ALK in an archive of lung adenocarcinoma ($n = 130$) and another 4 among fresh cases analyzed in a diagnostic laboratory. These 8 tumors were found to include 1 with *EML4-ALK* variant 1, 1 with variant 2, 3 with variant 3, and 2 with previously unidentified variants (designated variants 6 and 7). Inverse reverse transcription-PCR analysis revealed that the remaining tumor harbored a novel fusion in which intron 24 of *KIF5B* was ligated to intron 19 of *ALK*. Multiplex reverse transcription-PCR analysis of additional archival tumor specimens identified another case of lung adenocarcinoma positive for *KIF5B-ALK*.

Conclusions: The iAEP method should prove suitable for immunohistochemical screening of tumors positive for ALK or ALK fusion proteins among pathologic archives. Coupling of PCR-based detection to the iAEP method should further facilitate the rapid identification of novel ALK fusion genes such as *KIF5B-ALK*.

Gene fusion is a major mechanism of carcinogenesis in hematologic malignancies and sarcomas (1). Identification of the BCR-ABL fusion kinase, which is generated as a result of the balanced chromosome anomaly t(9;22)(q34;q11) in chronic myelogenous leukemia (2), has thus been followed by the discovery of many fusion-type oncogenes (3). In contrast, it has remained unclear whether such translocation-dependent fusion-type oncogenes also play a major role in the pathogenesis of epithelial tumors. Recently, however, almost 50% of prostate cancer cases have been suggested to harbor gene fusions involving ETS transcription factor loci (4), and we have discovered a recurrent chromosome translocation, inv(2)(p21p23), in non–small cell lung cancer (NSCLC) that results in the production of an EML4-ALK fusion-type protein tyrosine kinase (PTK; refs. 5–8).

Forced expression of EML4-ALK in lung epithelial cells induced the rapid development of hundreds of lung cancer nodules in mice, and peroral administration of inhibitors of the PTK activity of EML4-ALK was shown to clear such tumors from the lungs, demonstrating the pivotal role of EML4-ALK in the pathogenesis of NSCLC positive for this fusion kinase (9). This latter observation also supports the clinical application of ALK

Authors' Affiliations: [1]Division of Pathology, The Cancer Institute, Japanese Foundation for Cancer Research and [2]Department of Thoracic Surgical Oncology, Thoracic Center, Cancer Institute Hospital, Japanese Foundation for Cancer Research, Tokyo, Japan; [3]Division of Functional Genomics, Jichi Medical University, Tochigi, Japan; and [4]CREST, Japan Science and Technology Agency, Saitama, Japan

Received 12/15/08; revised 1/23/09; accepted 2/1/09; published OnlineFirst 4/21/09.

Grant support: Supported in part by Grants-in-Aid for Scientific Research from the Ministry of Education, Culture, Sports, Science, and Technology of Japan as well as by grants from the Japan Society for the Promotion of Science; the Ministry of Health, Labor, and Welfare of Japan; the National Institute of Biomedical Innovation of Japan; the Smoking Research Foundation of Japan; and the Vehicle Racing Commemorative Foundation of Japan.

The costs of publication of this article were defrayed in part by the payment of page charges. This article must therefore be hereby marked *advertisement* in accordance with 18 U.S.C. Section 1734 solely to indicate this fact.

Note: Supplementary data for this article are available at Clinical Cancer Research Online (http://clincancerres.aacrjournals.org/).

Current address of Y. Satoh: Department of Thoracic Surgery, Kitasato University School of Medicine, Kanagawa 228-8520, Japan.

Requests for reprints: Kengo Takeuchi, Division of Pathology, The Cancer Institute, Japanese Foundation for Cancer Research, Tokyo 135-8550, Japan. Phone: 81-3-3520-0111; Fax: 81-3-3570-0558; E-mail: kentakeuchi-tky@umin.net.

doi:10.1158/1078-0432.CCR-08-3248

Translational Relevance

Immunohistochemistry (IHC) is a reliable and relatively easy diagnostic tool to detect pathologic proteins in paraffin-embedded tissues. We have recently discovered an oncogenic fusion tyrosine kinase EML4-ALK in ~5% of non–small cell lung cancer cases. In contrast to the sensitive detection of other ALK fusions, such as NPM-ALK in anaplastic large cell lymphoma, however, IHC-mediated identification of EML4-ALK has been difficult, probably owing to the low expression level of the protein. To overcome such limitation, we here developed an intercalated antibody-enhanced polymer (iAEP) method, which is simple, yet provides high sensitivity in the IHC-mediated detection of EML4-ALK. With iAEP, in addition to the faithful detection of all non–small cell lung cancer specimens known to be positive for EML4-ALK, we have further identified specimens carrying novel variants of EML4-ALK or an unknown oncogenic fusion, KIF5B-ALK. Therefore, iAEP would provide a reliable and sensitive means to detect ALK fusions in human cancers.

inhibitors (6, 10) to treat EML4-ALK–positive lung cancer in humans. It should be noted, however, that multiple isoforms of EML4-ALK, generated mainly as a result of diversity in the breakpoint-fusion point within *EML4* (6, 8, 11, 12), have been identified in NSCLC specimens. The accurate diagnosis of *EML4-ALK*–positive tumors will therefore require detection of all in-frame fusions between *EML4* and *ALK* cDNAs, as exemplified by our multiplex reverse transcription– and PCR-based detection system for *EML4-ALK* (8).

Given that, in many pathology laboratories, most specimens submitted for histopathologic diagnosis are stored as formalin-fixed, paraffin-embedded tissue, the DNA or RNA of which may be substantially degraded, it is desirable to develop a suitable and sensitive means to detect EML4-ALK in such samples. An immunohistochemistry-based diagnostic system is one potential approach to such screening. In contrast to the efficient detection of NPM-ALK fusion proteins in anaplastic large cell lymphoma specimens with such an approach (13), however, many researchers have encountered difficulty in detecting ALK fusion proteins in lung tissue by immunohistochemical analysis (14), possibly as a result of weak transcriptional activity of the promoter-enhancer region of *EML4* that drives the expression of *EML4-ALK* compared with that of the *NPM* promoter. We have now attempted to establish a sensitive screening system for ALK fusion protein–positive tumors with an immunohistochemical approach. Furthermore, with such an approach, we unexpectedly discovered a novel *ALK* fusion gene, *KIF5B-ALK*, in NSCLC.

Materials and Methods

Samples. As a test set of samples for the development of sensitive immunohistochemical detection of EML4-ALK, we examined specimens from 11 patients with NSCLC positive for *EML4-ALK* (previously analyzed in ref. 8) and 10 patients with NSCLC negative for the fusion

Table 1. Immunohistochemical staining of EML4-ALK–positive or EML4-ALK–negative NSCLC specimens and quantitation of *ALK* mRNA

Tumor ID	EML4-ALK variant	Staining intensity						*ALK* mRNA level	
		ALK1	ALK1 with iAEP	5A4	5A4 with iAEP	SP8	SP8 with iAEP	5′ region	3′ region
#4808	V1	-	+	-	+	-	+	1.3	57.3
#9034	V1	-	++	+	++	-/+	++	0	83.3
#9968	V1	-	+	-	+	-	+	15.9	150.1
#2374	V2	-	++	-/+	++	-/+	++	1	182.3
#3121	V2	-	++	-/+	++	-/+	++	0	118.6
#4180	V2	-	++	-/+	++	-/+	++	1.4	124.5
#2075	V3	-	++	-/+	++	-/+	++	7	72
#7969	V3	+	+++	++	+++	+	++	3.6	52.7
#9616	V3	-/+	++	+	++	+	++	5.7	33.8
#8398	V4	-	++	-/+	++	-/+	++	0	118.6
#8993	V5	-	++	-/+	++	-/+	++	1.1	61.4
NC #1	NA	-	-	-	-	-	-/+	1	1
NC #2	NA	-	-	-	-	-	-/+	1.2	5.5
NC #3	NA	-	-	-	-	-/+	+	0.9	8.8
NC #4	NA	-	-	-	-/+	-/+	++	4.1	1.4
NC #5	NA	-	-	-	-	-	+	0.6	2.2
NC #6	NA	-	-	-	-	-	+	0.3	1.1
NC #7	NA	-	-	-	-	-/+	+	4.8	2.7
NC #8	NA	-	-	-	-	-	+	1.7	3.8
NC #9	NA	-	-	-	-	-	+	1.5	3.3
NC #10	NA	-	-	-	-/+	-/+	++	2.5	3

NOTE: Tumor specimens of the test cohort were subjected to immunohistochemical staining with the antibody preparations ALK1, 5A4, or SP8 according to the standard protocol or by the iAEP method. Staining intensity is represented as follows: +++, strongly positive; ++, positive; +, weakly but definitely positive; -/+, indeterminate; -, negative. The abundance of ALK mRNA in the specimens was determined by real-time RT-PCR analysis with the primers targeted to the 5′ or 3′ regions, which correspond to the extracellular and intracellular portions, respectively, of ALK; data are normalized relative to the NC (negative control) #1 specimen.
Abbreviation: NA, not applicable.

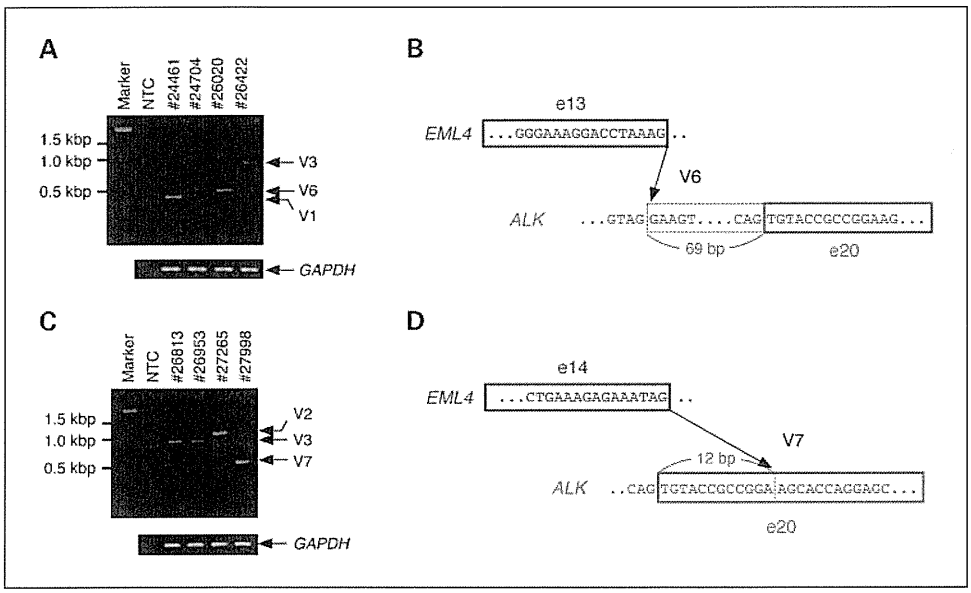

Fig. 1. Identification of novel variants of *EML4-ALK*. *A,* multiplex RT-PCR analysis of all possible in-frame fusions between *EML4* and *ALK* was done with the four specimens of lung adenocarcinoma in the validation cohort that were positive for immunostaining with 5A4 by the iAEP method (*top*). In addition to the detection of *EML4-ALK* variants (*V*)1 and 3 in tumor IDs #24461 and #26422, respectively, a novel PCR product (variant 6) was obtained with tumor ID #26020, whereas no product was obtained with tumor ID #24704. The *GAPDH* cDNA was also amplified as a control for each specimen (*bottom*). Tumor Ids (*top*) and the size of DNA markers (*bottom*; 100-bp ladder) are shown. *Right,* the positions of *EML4-ALK* variants and the PCR product for *GAPDH*. *NTC,* no-template control. *B,* fusion point for *EML4-ALK* variant 6 cDNA. Exon (*e*) 13 of *EML4* is fused to intron 19 of *ALK* at a position 69 bp upstream of exon 20. *C,* multiplex RT-PCR analysis as in *A* for the 4 specimens of lung adenocarcinoma that were identified as positive for immunostaining with 5A4 by the iAEP method in routine diagnostic screening. Tumor IDs #26813 and #26953 were shown to be positive for variant 3 of *EML4-ALK*, whereas #27265 was positive for variant 2. Tumor ID #27988 yielded a PCR product corresponding to a novel variant (variant 7) of *EML4-ALK*. *D,* fusion point of *EML4-ALK* variant 7 cDNA. Exon 14 of *EML4* is fused to nucleotide 13 of exon 20 of *ALK*.

gene. The former cohort comprised 3 cases each for EML4-ALK variants 1, 2, and 3 as well as one case each for variants 4 and 5. As a validation set of samples, we examined specimens from 130 consecutive patients with lung adenocarcinoma, from whom written informed consent was obtained. All specimens were collected with the approval of the ethics committee at the Cancer Institute Hospital (Tokyo, Japan), and the study was approved by the institutional review board of the Japanese Foundation for Cancer Research. Surgically removed cancer specimens were routinely fixed in 20% neutralized formalin and embedded in paraffin. Total RNA was extracted from the corresponding snap-frozen specimens and purified with the use of an RNeasy Mini kit (Qiagen).

Intercalated antibody-enhanced polymer method. Formalin-fixed, paraffin-embedded tissue was sliced at a thickness of 4 μm, and the sections were placed on silane-coated slides. Five antibody preparations specific for the intracellular region of ALK (ALK1 from Dako, 5A4 and SP8 from Abcam, ZAL4 from Zymed, and p80 from Nichirei) were evaluated for immunohistochemical staining according to standard protocols with the use of a dextran polymer reagent (anti-rabbit or anti-mouse immunoglobulin EnVision+DAB system; Dako). On the basis of their reactivity in such experiments, three antibodies (ALK1, 5A4, and SP8) were selected for development of the intercalated antibody-enhanced polymer (iAEP) method as follows. For antigen retrieval, the slides were heated for 40 min at 97°C in Target Retrieval Solution (pH 9.0; Dako). They were then incubated at room temperature first with Protein Block Serum-free Ready-to-Use solution (Dako) for 10 min and then with antibodies to ALK for 30 min. To increase the sensitivity of detection, we included an incubation step of 15 min at room temperature with rabbit polyclonal antibodies to mouse immunoglobulin (Dako) or mouse antibodies to rabbit immunoglobulin (Dako), as appropriate. The immune complexes were then detected with the dextran polymer reagent and an AutoStainer instrument (Dako).

Detection of *EML4-ALK* and *KIF5B-ALK* cDNAs and characterization of their protein products is described in Supplementary Methods.

Results

Development of the iAEP method. A specimen of NPM-ALK–positive anaplastic large cell lymphoma was subjected to immunohistochemical staining with 5 different antibody preparations specific for ALK (ALK1 at a 1:20 dilution, 5A4 at 1:50, SP8 at 1:100, ZAL4 at 1:200, or p80 at 1:100) by the EnVision+DAB polymer method. All antibody preparations stained both the nucleus and cytoplasm of the lymphoma cells, whereas ZAL4 also reacted with normal mesenchymal cells (data not shown). In addition, the staining intensity with p80 was relatively low. We therefore selected ALK1, 5A4, and SP8 for initial development of a detection system for EML4-ALK.

Immunohistochemical analysis of a test set of samples (11 specimens of *EML4-ALK*–positive NSCLC and 10 specimens of *EML4-ALK*–negative NSCLC) with these 3 antibody preparations revealed negative to marginally positive reactivity with EML4-ALK by a conventional staining protocol based on the EnVision+DAB system (Supplementary Fig. S1; Table 1). We therefore incorporated an intercalating antibody before the EnVision+DAB system and applied this iAEP method to the same set of specimens. All three antibody preparations detected EML4-ALK in all *EML4-ALK*–positive cases in the test cohort (Supplementary Fig. S1; Table 1). However, SP8 also reacted with most of the *EML4-ALK*–negative specimens (Supplementary Fig. S2; Table 1), rendering it unsuitable for large-scale screening. Furthermore, a low level of nonspecific background staining of nontumor cells was apparent in all sections stained with ALK1.

We selected ALK1 and 5A4 for examination of a validation set of samples (a consecutive series of 130 lung adenocarcinoma

specimens). Four cases of this cohort were positive for staining with both antibodies by the iAEP method. Again, most of the other specimens also showed a low level of background staining with ALK1, whereas only a few did so with 5A4. We therefore selected 5A4 to detect EML4-ALK with the iAEP method and included this approach in our routine diagnostic service at the pathology division of The Cancer Institute during the study period, thereby identifying four additional cases of lung adenocarcinoma positive for staining with 5A4.

Identification of variants 6 and 7 of **EML4-ALK.** The four specimens recognized by 5A4 in the validation set (IDs #24461, #24704, #26020, and #26422) were examined for the presence of *EML4-ALK* transcripts with our multiplex reverse transcription-PCR (RT-PCR) screening system, which was designed to capture all possible in-frame fusions between *EML4* and *ALK* at the cDNA level (8). Three cases (#24461, #26020, and #26422) were positive for *EML4-ALK* cDNAs (Fig. 1A), and nucleotide sequencing of the PCR products revealed that #24461 and #26422 tumors harbored variants 1 and 3 of *EML4-ALK*, respectively. The cDNA derived from tumor #26020, however, contained exon 13 of *EML4* as well as a portion of intron 19 and exon 20 of *ALK*, corresponding to a previously unidentified fusion variant (designated variant 6) of *EML4* and *ALK* (Supplementary Fig. S3A; Fig. 1B). The fusion of exon 13 of *EML4* to a position 69 bp upstream of exon 20 of *ALK* in this fusion cDNA would be expected to constitute an in-frame fusion between the two genes. Although there were no reported mRNAs or expressed sequence tags containing intron 19 of *ALK* in the sequence databases, the genomic sequence surrounding the fusion point in this intron is AG-GA (Fig. 1B), which conforms to the consensus sequence for a splicing acceptor site, suggesting that this position of intron 19 may act as a cryptic acceptor site for RNA splicing.

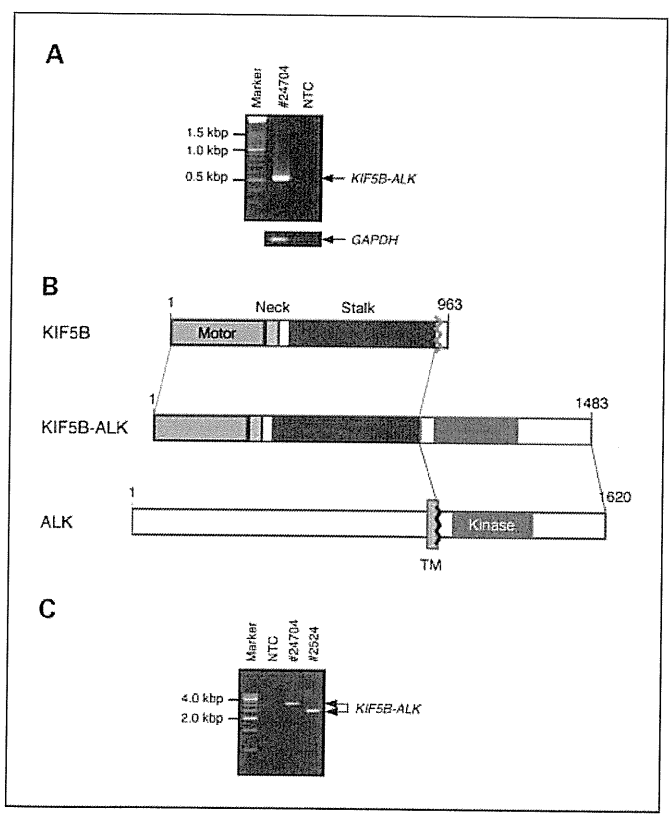

Fig. 2. Discovery of a *KIF5B-ALK* fusion gene associated with lung cancer. *A*, RT-PCR analysis of tumor ID #24704 with a forward primer targeted to exon 24 of *KIF5B* and a reverse primer targeted to exon 20 of *ALK*. Marker, 100-bp ladder. *B*, structure of KIF5B-ALK. KIF5B consists of an amino terminal ATP-dependent motor domain followed by a neck region and a stalk region containing seven coiled-coil domains. A chromosome translocation, t(2;10)(p23;p11), generates a fusion protein in which the entire motor domain and neck and stalk regions of KIF5B are joined to the intracellular region of ALK (containing the tyrosine kinase domain). Numbers indicate amino acid positions of each protein. *TM*, transmembrane domain. *C*, PCR analysis of genomic DNA from tumors #24704 and #2524 with primers flanking the putative fusion point of *KIF5B-ALK*. Marker, 500-bp ladder.

Similar analysis by multiplex RT-PCR and sequence determination revealed that the additional 4 ALK-positive cases identified by our routine pathologic diagnostic service comprised one case (tumor ID #27265) with variant 2 of *EML4-ALK*, 2 cases (#26813 and #26953) with variant 3, and 1 case (#27998) with another novel variant (designated variant 7), in which exon 14 of *EML4* is fused to nucleotide 13 of exon 20 of *ALK* (Supplementary Fig. S3B; Fig. 1C and D). Genomic PCR analysis of the specimens positive for variants 6 and 7 of *EML4-ALK* cDNA confirmed the presence of genomic rearrangements responsible for the fusion events detected at the cDNA level (data not shown).

Identification of **KIF5B-ALK** *as a novel* **ALK** *fusion gene.* Whereas tumor #24704 of the validation cohort was strongly positive for ALK immunostaining by the iAEP method, multiplex RT-PCR analysis failed to amplify a specific product from this sample. We therefore examined the possibility that this tumor might harbor an *ALK* fusion gene other than *EML4-ALK*. We subjected the sample to an inverse RT-PCR analysis and obtained a PCR product containing both exon 24 of *KIF5B* and exon 20 of *ALK*. *KIF5B* is located on the short arm of human chromosome 10 and encodes member 5B of the kinesin family of proteins. To confirm the presence of a *KIF5B-ALK* fusion gene in this tumor, we directly amplified the fusion point of the *KIF5B-ALK* cDNA by RT-PCR with one primer targeted to exon 24 of *KIF5B* and the other to exon 22 of *ALK*. A single PCR product with the expected size of 546 bp was obtained (Fig. 2A). Nucleotide sequencing of the product further confirmed the fusion point of *KIF5B-ALK* at the cDNA level (data not shown).

KIF5B is a component of a motor protein complex that is associated with microtubules and mediates the transport of organelles within eukaryotic cells (15). It consists of an amino terminal motor domain followed by a neck region and a stalk region, the latter of which directly mediates homodimerization of KIF5B (Fig. 2B). Fusion of exons 1 to 24 of *KIF5B* to exon 20 of *ALK* would be expected to result in the production of a fusion protein consisting of almost the entire KIF5B sequence ligated to the intracellular region of ALK. It might therefore also be expected that KIF5B-ALK would undergo homodimerization mediated by the stalk region of KIF5B, with consequent activation of the kinase function of ALK, similar to the case of EML4-ALK, in which homo-oligomerization and activation are mediated by the amino terminal coiled-coil domain of EML4 (5, 8).

We next modified our multiplex RT-PCR method so that it could detect both *EML4-ALK* and *KIF5B-ALK* fusion mRNAs. In addition to a forward primer targeted to the boundary of exons 23 and 24 of *KIF5B* (to amplify the identified *KIF5B-ALK* fusion point), we included another forward primer targeted to exon 10 of *KIF5B* to detect potential novel fusion cDNAs for

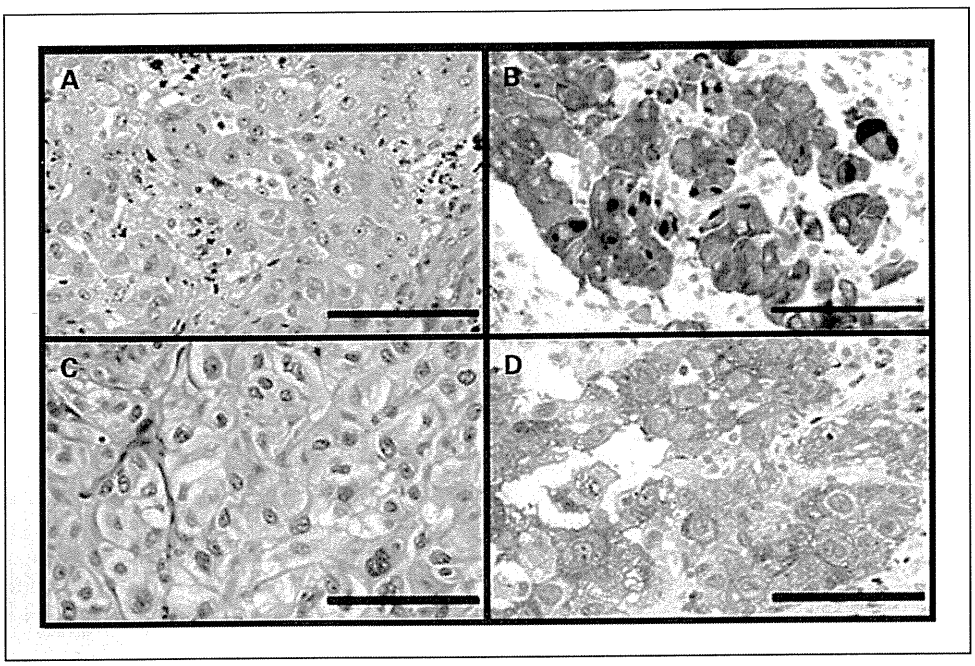

Fig. 3. Histopathology of KIF5B-ALK–positive lung adenocarcinoma. Sections of tumors #24704 (*A* and *B*) and #2524 (*C* and *D*) ware stained with H&E (*A* and *C*) or subjected to immunohistochemical analysis with 5A4 by the iAEP method (*B* and *D*). Some cancer cells of tumor #24704 contained intracytoplasmic macroglobular spots strongly positive for KIF5B-ALK (*B*). Some tumor cells showed a perinuclear halo positive for KIF5B-ALK (*D*). *Scale bars,* 100 μm.

KIF5B-ALK proteins containing a partial stalk region of KIF5B (given that the stalk region contains seven coiled-coil domains, a partial stalk region may still allow homodimerization of KIF5B-ALK). This newly designed multiplex RT-PCR assay was then applied both to the eight specimens found in this study to harbor *EML4-ALK* (7 cases) or *KIF5B-ALK* (#24704) and to the panel of cancer specimens including 253 samples of lung adenocarcinoma, 111 samples of other types of lung cancer, and 292 samples of tumors from 10 other organs, which was studied previously (8). Our modified multiplex RT-PCR method detected all 8 cases shown to be positive for *EML4-ALK* or *KIF5B-ALK* in the present study as well as 11 cases known to harbor various *EML4-ALK* fusion genes in the previous cohort (data not shown). The modified multiplex RT-PCR assay also identified one case (#2524) of lung adenocarcinoma harboring *KIF5B-ALK* among the previous cohort. We thus identified two cases positive for *KIF5B-ALK* among a total of 383 cases of lung adenocarcinoma (2 of 383 = 0.52%). Genomic rearrangement responsible for the identified *KIF5B-ALK* cDNAs was also confirmed in these two cases by genomic PCR analysis. The PCR products differed between the 2 cases, indicative of distinct breakpoints and fusion points within intron 24 of *KIF5B* and intron 19 of *ALK* (Fig. 2C).

Histopathology of* KIF5B-ALK*–positive lung adenocarcinoma. Histopathologic analysis of the two cases of *KIF5B-ALK*–positive lung adenocarcinoma revealed papillary structures, whereas the acinar pattern with prominent mucin production typically apparent in *EML4-ALK*–positive cases (7) was rarely observed. The individual cancer cells contained abundant eosinophilic cytoplasm and a large vesicular nucleus with one or two prominent nucleoli, and they were generally larger than those observed in *EML4-ALK*–positive cases (Supplementary Fig. S4A; Fig. 3A and C). Lymphatic invasion was prominent in tumor #24704, and the tumor cells in the lymphatic vessels contained an eccentric nucleus and a perinuclear eosinophilic globule (Supplementary Fig. S4A). Immunohistochemical detection of KIF5B-ALK with 5A4 by the iAEP method revealed a diffuse cytoplasmic staining in all of the cancer cells. Some cells manifested an uneven staining profile, with a perinuclear halo (Supplementary Fig. S4B; Fig. 3D) or macroglobular spots (Fig. 3B), neither of which was observed in tumors positive for EML4-ALK (8).

Fluorescence* in situ *hybridization analysis of* KIF5B-ALK*–positive tumors. To confirm further the genomic rearrangement in the two tumors positive for *KIF5B-ALK*, we did three fluorescence *in situ* hybridization assays: an *ALK* split assay, a *KIF5B* split assay, and a *KIF5B-ALK* fusion assay. The results for all three assays were consistent with the presence of a t(2;10)(p23;p11) responsible for the generation of *KIF5B-ALK* (Fig. 4). Cancer cells of tumor #24704 thus exhibited one isolated 3′-*ALK* signal and one isolated 5′-*KIF5B* signal in the *ALK* split assay and the *KIF5B* split assay, respectively, whereas they manifested one merged signal in the *KIF5B-ALK* fusion assay. Cancer cells of tumor #2524 exhibited at least two merged signals, indicative of possible amplification of the fusion gene. Neither an isolated 3′-*KIF5B* signal nor an isolated 5′-*ALK* signal was detected in the split assays for either case, suggesting that the derivative chromosome 2 harboring the *ALK-KIF5B* fusion gene may have been deleted after the balanced translocation between chromosomes 2 and 10.

Transforming activities of EML4-ALK variants 6 and 7 and of KIF5B-ALK. To isolate full-length cDNAs for the new variants of *EML4-ALK*, we did RT-PCR analysis with a forward primer targeted to the 5′ untranslated region of *EML4* cDNA and a reverse primer targeted to the 3′ untranslated region of *ALK* cDNA as described previously (6, 8). From oligo(dT)-primed cDNA preparations of tumor IDs #26020 or #27998, we isolated cDNAs of 3365 and 3435 bp, corresponding to variants 6 and 7 of *EML4-ALK*, respectively (data not shown). Similarly, a full-length cDNA of 4479 bp for *KIF5B-ALK* was obtained by RT-PCR analysis from tumor ID #2524. Nucleotide sequencing of these cDNAs confirmed that each of them would be expected to produce a functional PTK, with a predicted molecular size of 119,380 Da for EML4-ALK variant 6 (Supplementary Fig. S3A),

122,220 Da for EML4-ALK variant 7 (Supplementary Fig. S3B), and 167,903 Da for KIF5B-ALK (Supplementary Fig. S5).

Recombinant retroviruses encoding each of these fusion PTKs were generated and used to infect cultured 3T3 fibroblasts. Infection with the viruses encoding EML-ALK variant 6, EML4-ALK variant 7, or KIF5B-ALK, but not that with the empty virus, resulted in the formation of dozens of transformed foci *in vitro* (Fig. 5). As positive controls for focus formation, EML4-ALK variant 1 and NPM-ALK each yielded a similar number of transformed foci.

The same set of 3T3 cells was injected into nude mice for an *in vivo* tumorigenicity assay. All fusion PTKs induced s.c. tumors at all injection sites within an observation period of 20 days (Fig. 5), confirming the transforming potential of the novel variants of EML4-ALK as well as that of KIF5B-ALK.

Discussion

Immunohistochemical detection of ALK fusion proteins has been applied successfully to analysis of anaplastic large cell lymphoma and inflammatory myofibroblastic tumors, with the mouse monoclonal antibody ALK1 being most widely used for this purpose. However, many researchers were not able to reliably detect EML4-ALK in NSCLC specimens with this same immunohistochemical technique (14). Even if NSCLC specimens were positive for such staining, its intensity was usually low and varied substantially among sections of the same tumor, rendering the current standard technique unsuitable for screening of NSCLC specimens. This low sensitivity for the detection of EML4-ALK may be attributable to the low level of *EML4* transcriptional activity (see, for example, a public database for serial analysis of gene expression)[5] or to instability of EML4-ALK in cells.

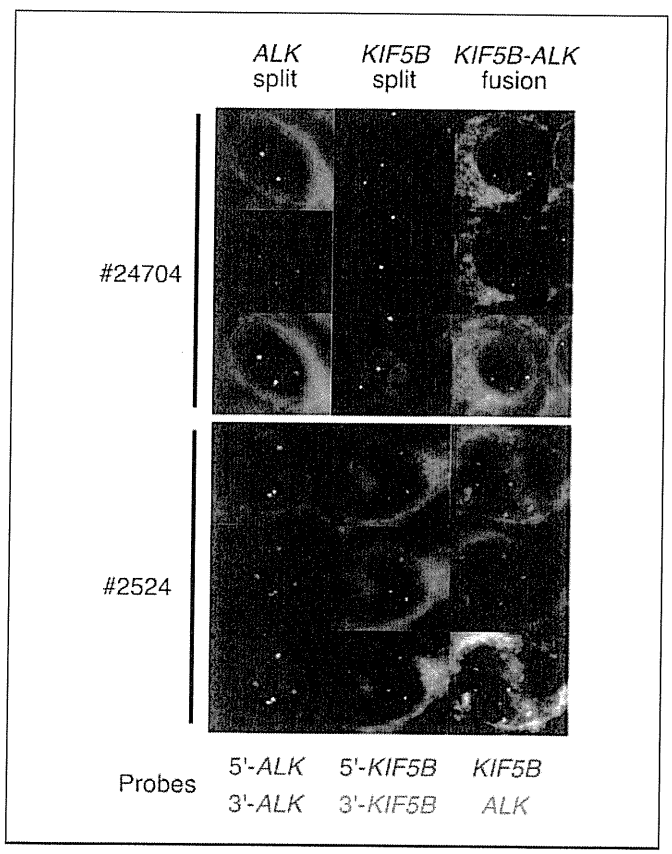

Fig. 4. Fluorescence *in situ* hybridization analysis of *KIF5B-ALK*. Sections of tumors positive for *KIF5B-ALK* (IDs #24704 and #2524) were subjected to fluorescence *in situ* hybridization with an *ALK* split assay (*left*), a *KIF5B* split assay (*middle*), or a *KIF5B-ALK* fusion assay (*right*). *Bottom*, the color of fluorescence for the BAC clones in each hybridization. Nuclei are stained blue with 4',6-diamidino-2-phenylindole.

However, given that immunohistochemical analysis is a convenient means to detect a protein of interest in pathology laboratories, it is desirable to establish a sensitive and accurate screening system for ALK fusion proteins based on this approach. Several candidate techniques with improved sensitivity, such as tyramide signal amplification (16), have been recently proposed. These techniques generally require multiple steps, however, which can compromise reproducibility and render them unsuitable for screening in routine pathologic diagnosis.

We have now achieved a moderate increase in the sensitivity of immunohistochemical detection of ALK fusion proteins by including antibodies to mouse or rabbit immunoglobulin as an intercalating reagent between the primary antibody and the EnVision+DAB polymer detection system. This iAEP method allowed the detection of EML4-ALK fusion proteins in all 11 specimens positive for *EML4-ALK* in our test cohort. This simple method can be readily done in ordinary diagnostic pathology laboratories. Although we selected the mouse monoclonal antibody 5A4 for immunohistochemistry by the iAEP method, other antibodies may be more suitable for routine diagnostic analysis with a modified version of this approach.

All antibodies used in the present study are specific for the intracellular region of ALK and so would be expected to detect both EML4-ALK and wild-type ALK. It is therefore possible that positive staining with 5A4 by the iAEP method does not reflect only the presence of ALK fusion proteins. To address this issue, we determined the amount of *ALK* mRNA with primers targeted to the 5′ or 3′ regions of *ALK* cDNA separately (whereas the latter would be expected to amplify cDNAs for both wild-type *ALK* and *ALK* fusion genes, the former would be expected to amplify only that of wild-type *ALK*). None of the *EML4-ALK*–positive specimens in the test set of samples yielded a substantial amount of wild-type *ALK* cDNA (although tumor #9968 may express the wild-type gene at a low level), suggesting that our iAEP method with 5A4 detected EML4-ALK proteins rather than wild-type ALK in the positive specimens. For ALK-rich tissues such as the brain or spinal cord (17), however, it would be important to determine which proteins are recognized by 5A4 in iAEP analysis.

We identified 8 tumors positive for staining with 5A4 by the iAEP method among the validation set of samples (n = 130) and the fresh cases subjected to routine diagnostic testing. Although 5 of these specimens harbored known EML4-ALK variants, the remaining three were found to express novel ALK fusion proteins, including EML4-ALK variants 6 (#26020) and 7 (#27998) and KIF5B-ALK (#24704). These results thus showed that sensitive immunohistochemical analysis was superior to PCR-based methods for detecting novel ALK fusion constructs among tumor specimens. This conclusion was further supported by the fact that neither *EML4-ALK* nor *KIF5B-ALK* was identified in the iAEP-negative cases by our modified multiplex RT-PCR assay (data not shown).

[5] http://cgap.nci.nih.gov/sage/anatomicviewer

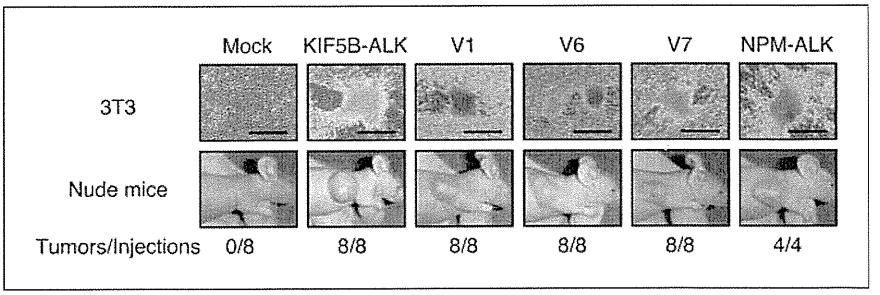

Fig. 5. Transforming activities of EML4-ALK and KIF5B-ALK. *A,* mouse 3T3 fibroblasts were infected with retroviruses encoding KIF5B-ALK, NPM-ALK, or variant 1, 6, or 7 of EML4-ALK or with the corresponding empty virus (*mock*). The cells were photographed after culture for 14 d. *Scale bars,* 500 μm. *B,* nude mice were injected s.c. with 3T3 cells infected as in *A*, and tumor formation was examined after 20 d. *Bottom,* the number of tumors formed per eight injections.

A fusion protein containing most of KIF5B and the intracellular (kinase) domain of the platelet-derived growth factor receptor A has been detected in idiopathic hypereosinophilic syndrome (18). The genome of some patients with this condition exhibits a chromosome translocation, t(4;10)(q12;p11), which results in the production of a *KIF5B-PDGFRA* fusion mRNA in which exon 23 of *KIF5B* is ligated to exon 12 of *PDGFRA*. Given that the KIF5B portion of KIF5B–platelet-derived growth factor receptor A contains six of the seven coiled-coil domains within the stalk region, the fusion protein likely dimerizes constitutively and thereby possesses transforming potential. KIF5B-ALK is thus the second example of an oncogenic KIF5B fusion to a PTK.

The subcellular localization of ALK fusion proteins likely depends on the fusion partner. For instance, whereas NPM-ALK, which is associated with anaplastic large cell lymphoma, is present in both the nucleus and cytoplasm, nuclear localization has not been detected for other ALK fusion proteins including CLTC-ALK, TPM3-ALK, TFG-ALK, ATIC-ALK (19), and EML4-ALK (5). The pattern of immunohistochemical staining for KIF5B-ALK did not resemble that of any of these other ALK fusion proteins. The observed perinuclear halo of KIF5B-ALK staining may indicate accumulation of the fusion protein at the periphery of the cytoplasm (subcell membrane region), possibly reflecting transport of KIF5B-ALK along microtubules. Signaling downstream of KIF5B-ALK may thus differ substantially from that of other ALK fusion proteins, as exemplified by the differential phosphorylation of STAT proteins associated with these fusion proteins (19).

In conclusion, we have developed a modified immunohistochemical staining procedure for the detection of ALK and ALK fusion proteins in lung cancer that may prove suitable for screening purposes in pathology laboratories. Our identification of a second ALK fusion gene, *KIF5B-ALK*, in NSCLC further supports the clinical relevance of *ALK* in the pathogenesis of this disease. Given the recent development of several ALK inhibitors and their potential therapeutic efficacy for tumors positive for ALK fusion proteins (6, 10, 20), accurate diagnosis of tumors expressing activated ALK or ALK fusion proteins (5, 21, 22) will be essential to identify subgroups of patients who are suitable for treatment with such drugs.

Disclosure of Potential Conflicts of Interest

K.T. serves as a consultant to Dako.

Acknowledgments

We thank Motoyoshi Iwakoshi, Keiko Shiozawa, Tomoyo Kakita and Reimi Asaka for their technical assistance. The nucleotide sequences of the cDNAs for EML4-ALK variants 6 and 7 and for KIF5B-ALK have been deposited in the DDBJ/European Molecular Biology Laboratory/Genbank databases under the accession numbers AB462411, AB462412, and AB462413, respectively.

References

1. Mitelman F. Recurrent chromosome aberrations in cancer. Mutat Res 2000;462:247–53.
2. Bartram CR, de Klein A, Hagemeijer A, et al. Translocation of c-ab1 oncogene correlates with the presence of a Philadelphia chromosome in chronic myelocytic leukaemia. Nature 1983;306:277–80.
3. Mitelman F, Johansson B, Mertens F. The impact of translocations and gene fusions on cancer causation. Nat Rev Cancer 2007;7:233–45.
4. Kumar-Sinha C, Tomlins SA, Chinnaiyan AM. Recurrent gene fusions in prostate cancer. Nat Rev Cancer 2008;8:497–511.
5. Soda M, Choi YL, Enomoto M, et al. Identification of the transforming EML4-ALK fusion gene in non-small-cell lung cancer. Nature 2007;448:561–6.
6. Choi YL, Takeuchi K, Soda M, et al. Identification of novel isoforms of the EML4-ALK transforming gene in non-small cell lung cancer. Cancer Res 2008;68:4971–6.
7. Inamura K, Takeuchi K, Togashi Y, et al. EML4-ALK fusion is linked to histological characteristics in a subset of lung cancers. J Thorac Oncol 2008;3:13–7.
8. Takeuchi K, Choi YL, Soda M, et al. Multiplex reverse transcription-PCR screening for EML4-ALK fusion transcripts. Clin Cancer Res 2008;14:6618–24.
9. Soda M, Takada S, Takeuchi K, et al. A mouse model for EML4-ALK-positive lung cancer. Proc Natl Acad Sci U S A 2008;105:19893–7.
10. McDermott U, Sharma SV, Dowell L, et al. Identification of genotype-correlated sensitivity to selective kinase inhibitors by using high-throughput tumor cell line profiling. Proc Natl Acad Sci U S A 2007;104:19936–41.
11. Rikova K, Guo A, Zeng Q, et al. Global survey of phosphotyrosine signaling identifies oncogenic kinases in lung cancer. Cell 2007;131:1190–203.
12. Koivunen JP, Mermel C, Zejnullahu K, et al. EML4-ALK fusion gene and efficacy of an ALK kinase inhibitor in lung cancer. Clin Cancer Res 2008;14:4275–83.
13. Cataldo KA, Jalal SM, Law ME, et al. Detection of t(2;5) in anaplastic large cell lymphoma: comparison of immunohistochemical studies, FISH, and RT-PCR in paraffin-embedded tissue. Am J Surg Pathol 1999;23:1386–92.
14. Martelli MP, Sozzi G, Hernandez L, et al. EML4-ALK rearrangement in non-small-cell lung cancer and non-tumor lung tissues. Am J Pathol 2009;174:661–70.
15. Sablin EP. Kinesins and microtubules: their structures and motor mechanisms. Curr Opin Cell Biol 2000;12:35–41.
16. McLachlan CS, Jusuf PR, Rummery N, et al. Tyramide signal amplification enhances the detectable distribution of connexin-43 positive gap junctions across the ventricular wall of the rabbit heart. Arch Histol Cytol 2003;66:359–65.
17. Pulford K, Morris SW, Turturro F. Anaplastic lymphoma kinase proteins in growth control and cancer. J Cell Physiol 2004;199:330–58.
18. Score J, Curtis C, Waghorn K, et al. Identification of a novel imatinib responsive KIF5B-PDGFRA fusion gene following screening for PDGFRA overexpression in patients with hypereosinophilia. Leukemia 2006;20:827–32.
19. Armstrong F, Duplantier MM, Trempat P, et al. Differential effects of X-ALK fusion proteins on proliferation, transformation, and invasion properties of NIH3T3 cells. Oncogene 2004;23:6071–82.
20. McDermott U, Iafrate AJ, Gray NS, et al. Genomic alterations of anaplastic lymphoma kinase may sensitize tumors to anaplastic lymphoma kinase inhibitors. Cancer Res 2008;68:3389–95.
21. Morris SW, Kirstein MN, Valentine MB, et al. Fusion of a kinase gene, ALK, to a nucleolar protein gene, NPM, in non-Hodgkin's lymphoma. Science 1994;263:1281–4.
22. Chen Y, Takita J, Choi YL, et al. Oncogenic mutations of ALK kinase in neuroblastoma. Nature 2008;455:971–4.

An Imaging-Based Rapid Evaluation Method for Complement-Dependent Cytotoxicity Discriminated Clinical Response to Rituximab-Containing Chemotherapy

Yuji Mishima,[1,2] Natsuhiko Sugimura,[1,5] Yuko Matsumoto-Mishima,[2,3] Yasuhito Terui,[1,2,3] Kengo Takeuchi,[4] Suzuka Asai,[2] Daisuke Ennishi,[3] Hiroaki Asai,[3] Masahiro Yokoyama,[3] Kiyotsugu Kojima,[5] and Kiyohiko Hatake[1,3]

Abstract

Purpose: Rituximab has greatly improved the efficacy of chemotherapy regimens for CD20-positive non-Hodgkin's lymphoma. However, although several mechanisms of action of rituximab have been identified, the exact therapeutic functions of these mechanisms remains to be clarified. In addition, there is no established prognostic marker to predict an individual response. This study verified the validity of *ex vivo* complement-dependent cytotoxicity (CDC) susceptibility as a predictor of pathologic tumor regression in patients undergoing rituximab-containing chemotherapy and examined whether CDC contributes to the mechanism of action of rituximab.

Experimental Design: A rapid assay system was established to evaluate the tumoricidal activity of rituximab using a living cell–imaging technique. We analyzed lymph node biopsies obtained from 234 patients with suspected lymphomas and estimated the association between CDC susceptibility and the response to rituximab-containing chemotherapy in diffuse large B-cell lymphoma and follicular lymphoma.

Results: This study revealed that CDC susceptibility of lymphoma cells freshly obtained from patients was strongly associated with response to rituximab-containing chemotherapy in both diffuse large B-cell lymphoma and follicular lymphoma. This correlation was not apparent in cases that received chemotherapy without rituximab.

Conclusions: The system that we have established allows a successful assessment of rituximab-induced CDC and can distinguish cases refractory to rituximab-containing chemotherapy. The association between CDC susceptibility and therapy response suggests that CDC is pivotal in the ability of chemotherapy including rituximab to induce remission.

Although rituximab can be combined with chemotherapies used in the treatment of non-Hodgkin's lymphoma, efficacy varies from patient to patient. In addition, no prognostic marker to predict individual response has been established to date. Several mechanisms of action have been proposed and tested *in vitro*, mainly in tumor cell lines (1–3). Through its human IgG_1 Fc domain, rituximab can activate cellular effectors for antibody-dependent cellular cytotoxicity (ADCC) or phagocytosis and can recruit serum proteins for complement-dependent cytotoxicity (CDC; ref. 4). Moreover, cross-linking of CD20 molecules on tumor cell lines has been reported to trigger apoptosis, as well as having an antiproliferative effect on some, but not all, cell lines (5, 6). Despite these insights, the mechanisms mediating tumor cell eradication *in vivo* are not well understood. Recently, analyses of FcγRIIIa polymorphisms have clearly shown that ADCC is one of the critical effector functions responsible for the clinical efficacy of therapeutic antibodies (7–9). The FcγRIIIa gene (*FCGR3A*) displays an allelic polymorphism that generates molecules containing either a phenylalanine (F) or a valine (V) at amino acid position 158, which is critical in mediating ADCC. A greater clinical response in patients with the FcγRIIIa allotype (FcgRIIIa-158V), which has a high affinity for human IgG_1, has been observed compared with results obtained from patients with the low-affinity allotype (FcγRIIIa-158F; ref. 10). These reports show the importance of ADCC in clinical outcomes. On the other hand, there are few reports that indicate a contribution to clinical effect in

Authors' Affiliations: [1]Olympus Bio-Imaging Laboratory, [2]Clinical Chemotherapy, Cancer Chemotherapy Center, [3]Department of Clinical Oncology and Hematology, Cancer Institute Hospital, [4]Department of Pathology, Cancer Institute of the Japanese Foundation for Cancer Research, Tokyo, Japan, and [5]Olympus Corporation, Ltd., Tokyo, Japan

Received 7/8/08; revised 1/27/09; accepted 2/9/09; published OnlineFirst 5/5/09.

Grant support: Scientific Research no. 19590170 from the Ministry of Education of Japan (Y. Mishima), Grant-in-aid for scientific research on priority area 'cancer' no. 12218226 from the Ministry of Education, Culture, Sports, Science and Technology of Japan (K. Hatake).

The costs of publication of this article were defrayed in part by the payment of page charges. This article must therefore be hereby marked *advertisement* in accordance with 18 U.S.C. Section 1734 solely to indicate this fact.

Note: Supplementary data for this article are available at Clinical Cancer Research Online (http://clincancerres.aacrjournals.org/).

Requests for reprints: Kiyohiko Hatake, Japanese Foundation for Cancer Research, 3-10-6, Ariake, Koto-ku, Tokyo, Japan. Phone: 81-3-3520-0111; Fax: 011-81-81-3-3570-0465; E-mail: khatake@jfcr.or.jp.

doi:10.1158/1078-0432.CCR-08-1536

Translational Relevance

For the prediction of the therapeutic efficacy of molecularly targeted medicines, it is ideal to evaluate the therapeutic mechanisms in individual patients. Therefore, it is highly significant to evaluate the drug functions in fresh tumor cells near *in vivo* conditions. To date, invasiveness and a great deal of time and effort have been unavoidable in such evaluations. In this study, we developed a rapid evaluation system for complement-dependent cytotoxicity of rituximab by using living cell–imaging technology. The advantages of imaging-based procedures include the need for only a minimal amount of specimen as well as its rapidity. Our system enabled reproducible evaluation even from tiny specimens and distinguished between responsive and refractory groups of rituximab-containing chemotherapy. This evaluation system may be easy to apply to antibody medicines other than rituximab and to other mechanism of actions such as antibody-dependent cellular cytotoxicity. Thus, this study may offer the opportunity to evaluate the effect of various antibody drugs in clinical applications.

the mechanisms, apart from ADCC. Several reports have suggested the role of CDC in the clinical efficacy of rituximab (11-13); however, it is a less convincing argument than that for ADCC. To elucidate this question, it is absolutely critical to evaluate the intrinsic CDC susceptibility of freshly obtained lymphoma cells from patients. To do so, a rapid, reproducible, and sufficiently smaller-scaled assay system is essential. To address this, we established a novel procedure to quantify the susceptibility of patient-derived lymphoma cells to CDC induced by rituximab. We developed a remarkably smaller-scaled assay procedure by using a real-time imaging technique, making it possible to perform multiple measurements with a small portion of the cells derived from lymph node biopsy obtained for diagnosis. In this study, we evaluated the CDC susceptibility of 234 patients with suspected lymphoma, using this new analytic method. Among these cases, as for diffuse large B-cell lymphoma (DLBCL) and follicular lymphoma (FL) in which rituximab-containing chemotherapy is frequently chosen, we further evaluated how much CDC is involved in the therapeutic response.

Materials and Methods

Lymphoma cells from patients. Primary malignant lymphocytes were prepared from lymph node biopsy specimens obtained from patients who had given written informed consent. Briefly, an excised lymph node was minced with scissors, and a mononuclear cell fraction was obtained by centrifugation (1,000 × *g* at 25°C for 30 min) through Ficoll histopaque (Sigma). B-lymphoid tumor cells were further purified by immunomagnetic cell sorting (according to the manufacturer's instructions) using an anti-human CD19 antibody conjugated to magnetic beads (MACS System, Miltenyi Biotec) from a small part of the mononuclear cells. The study was approved by the Institutional Review Board of the Japanese Foundation for Cancer Research.

Antibodies. Rituximab was purchased from Chugai Pharmaceutical Co., Ltd., and dialyzed thrice into PBS. For a control study, the $F(ab')_2$ fragment of rituximab was prepared by treating the antibody with immobilized pepsin and separating the resulting $F(ab')_2$ fragments on an immobilized protein A column (Pierce Biotechnology, Inc.). Purified rituximab and its $F(ab')_2$ fragment were labeled with Alexa 488 (Molecular Probes) according to the manufacturer's instructions. FITC-labeled anti-human CD19 mouse monoclonal antibody and PE-labeled anti-CD20 mouse monoclonal antibody were purchased from Becton Dickinson for flow cytometry analysis. Anti-human CD19 Microbeads were purchased from Miltenyi Biotec for immunomagnetic cell sorting.

Live cell imaging-based CDC assay. Forty thousand purified B-lymphoid tumor cells were suspended in 4 μL of RPMI 1640 supplemented with 10% fetal bovine serum, 10 μg/mL of Alexa 488–labeled rituximab, and 5 μg/mL of propidium iodide (PI). The cell suspension was pipetted into a well made of silicon, 2.5 mm in diameter and 2 mm in depth, on a piece of cover glass. Subsequently, the cell suspension was set on the stage of a confocal microscope system (FV-1000; Olympus, Tokyo, Japan) set up in a microscope incubator (Tokken, Chiba, Japan). After 10 min of incubation, 1.0 μL of type AB human serum obtained from a healthy volunteer was added to the well. Cellular alteration immediately after the addition of serum was recorded every 4 s by a time-lapse function at a resolution of 640 × 640 pixels. Using an excitation laser beam with a wavelength of 488 nm, cellular morphology by Nomarski interference contrast imaging, the binding of rituximab at a wavelength of 505 to 525 nm and the PI incorporation into the nuclei of dead cells at a wavelength of 610 to 640 nm were observed. The schema of the principle of this assay is illustrated in Fig. 1. CDC susceptibility index was calculated according to the following formula:

$$\text{CDC susceptibility index (\%)} = \frac{(\text{no. of dead cells at 10 min} - \text{no. of dead cells at 0 min})}{(\text{no. of total cells at 10 min} - \text{no. of dead cells at 0 min})} \times 100$$

Selection of cutoff scores for the CDC susceptibility index. Relevant cutoff scores for predicting therapeutic effect for the CDC susceptibility index were obtained by carrying out receiver-operating characteristic (ROC) curve analysis. In brief, plots of sensitivity and 1– specificity for therapy response were obtained for this index; the closest-to-(0,1) criterion identifies the threshold value.

Statistical procedures. Patients who responded to rituximab-containing chemotherapy were compared with those who were resistant to it. The association of therapy response with the CDC susceptibility index was analyzed using the two-sided Fisher's exact test. $P < 0.05$ was considered significant. A multiple logistic regression analysis was conducted to identify independent predictors of the clinical response to rituximab-containing chemotherapy. A step-down procedure based on a likelihood ratio test was applied, arranged in descending order of importance, with $P = 0.05$ for entry into the model and $P = 0.10$ for removal. Statistical analysis was done using the SPSS software package.

Results

Setting the conditions of the CDC assay. To set the conditions of the assay, CDC susceptibility analysis was done using B-cell NHL cell lines, Daudi, Raji, and Ramos, and by changing several variables. First, to determine the optimal concentration of rituximab, we assessed CDC with various concentrations of rituximab. As a source of complement, human serum at a final concentration of 20% was added to these cell lines suspended in culture medium containing rituximab at a range of 0 to 100 μg/mL. Then, cell death induced during the next 10 min was quantified. CDC reached a plateau at a concentration of >10 μg/mL of rituximab in either cell line (Fig. 2A). To optimize final serum concentration, we next did an assay using various concentrations of human serum with 10 μg/mL of

rituximab. Cell death induced by CDC increased serum concentration dependently, but CDC activity did not reach the plateau at the 0% to 20% level we examined (Fig. 2B). As it was difficult to add more than 20% serum because of the limitations of manipulation, we set the final serum concentration to 20% for subsequent analyses. As to reaction time, cell death in all lines reached a plateau within 10 min after the addition of 20% final concentration of human serum (Fig. 2C). Taking these results into account, we concluded that CDC susceptibility was calculated by measuring the cellular ratio killed in 10 min after the addition of human serum at a final concentration of 20% to the cells suspended in culture medium containing 10 μg/mL of rituximab. To confirm the capability of the assay with clinical specimens, eight cases of freshly obtained lymphoma cells were used to analyze the abovementioned condition. As shown in Fig. 2D, in all eight cases, the proportion of dead cells asymptotically approached a fixed value that varied according to the cases within 10 min. Additionally, under the presence of 10 μg/mL of Alexa 488–labeled human IgG used as a control, a significant increment of cell death was observed in neither case.

The assay system was designed to use a CD19-positive fraction as target cells to reduce the influence of effector cells in the biopsy specimens. To confirm the influence of the effector cells that might not be removed completely in the actual assay, the analysis was carried out using a *F*(ab′)2 fragment of rituximab or heat-inactivated serum. The results obtained from lymphoma cells derived from five patients with non-Hodgkin's lymphoma (two cases of DLBCL and three cases of FL) indicated that cell death was extremely decreased by replacing rituximab with its *F*(ab′)2 fragment or by heat-inactivation of serum. In both cases, a very small percentage of cells underwent necrotic or apoptotic cell death, but the increase of cell death was not statistically significant and was not more than that observed when human IgG was used as a substitute for rituximab (Supplemental Table S1). These results suggested that the cytotoxicity levels induced by effector cells were almost negligible in our assay system.

Patient characteristics. We evaluated the CDC susceptibility of cells derived from lymph node biopsies taken from 234 cases of suspected lymphoma. The diagnosis breakdown was DLBCL, 23.5%; FL, 20.9%; DLBCL with FL, 2.1%; mantle cell lymphoma, 3.4%; mucosa-associated lymphoid tissue, 4.7%; Burkitt's lymphoma, 0.9%; chronic lymphocytic leukemia/small lymphocytic lymphoma, 2.6%; and cases other than B-cell non-Hodgkin's lymphoma, 42.7%. The cases other than B-cell non-Hodgkin's lymphoma included T-cell lymphomas, nonneoplastic lymph proliferative diseases, lymphadenitis, and Hodgkin's disease. The samples evaluated included 51 patients with DLBCL and 45 patients with FL; patient characteristics are shown in Table 1. Cases were excluded in which

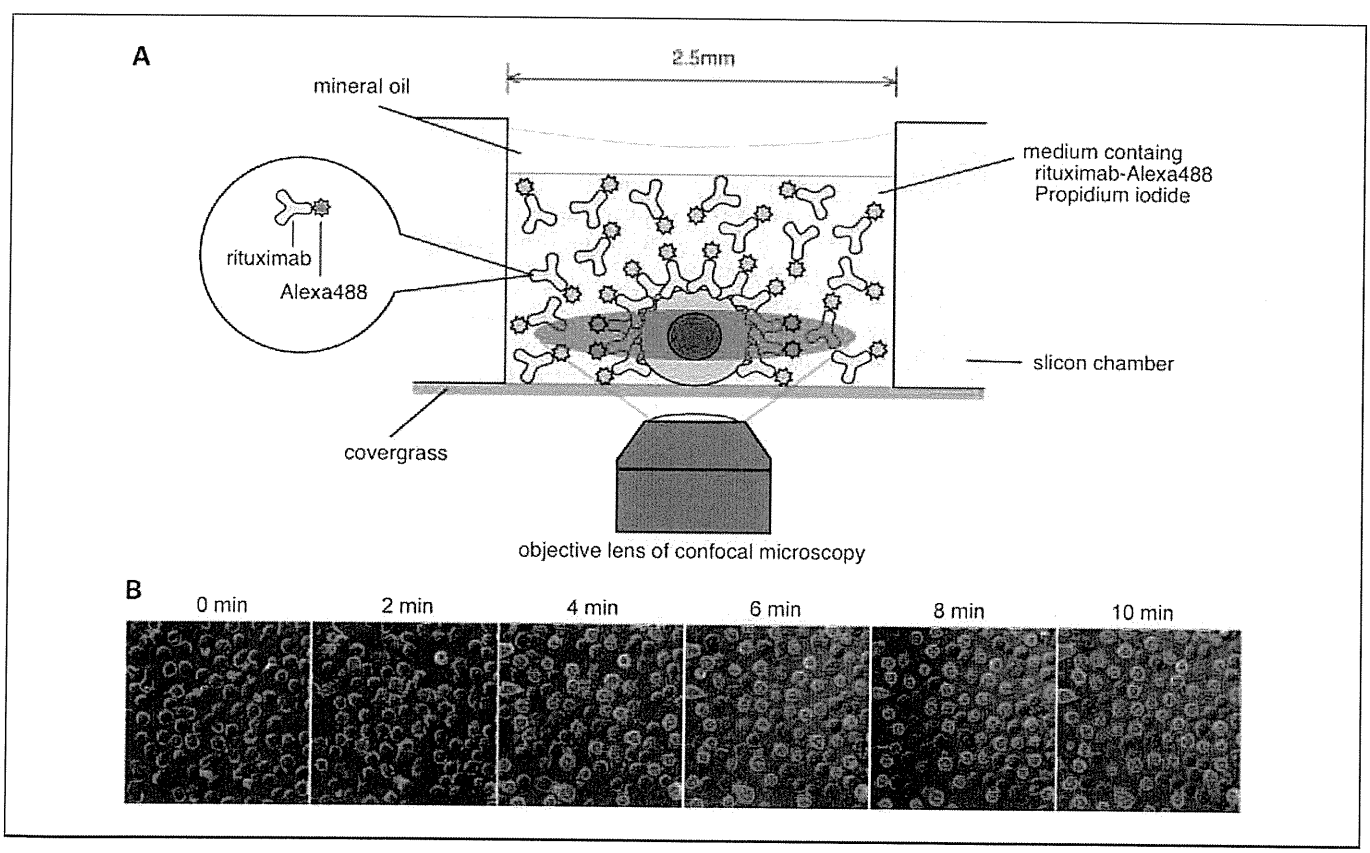

Fig. 1. The principle of imaging-based CDC susceptibility assay. *A*, a schema of CDC susceptibility assay based on living cell imaging. Lymphoma cells were suspended in 4 μL of culture medium containing Alexa 488–labeled rituximab and propidium iodide. The alteration of cellular viability from immediately after the addition of 1 μL of human serum was observed. The CDC-mediated cell killing was distinguished by the incorporation of PI into the nuclei. The background noise from the fluorescent antibody that existed in the culture medium could be excluded by detecting only fluorescent signals around a cellular equatorial plane by using confocal technology. *B*, an example of the assay results from a patient with FL lymphoma. Typical analysis results were shown extracting to images of every 120 s. Green signals, Alexa 488–labeled rituximab; red signals, incorporation of PI into nuclei; bar, 10 μm.

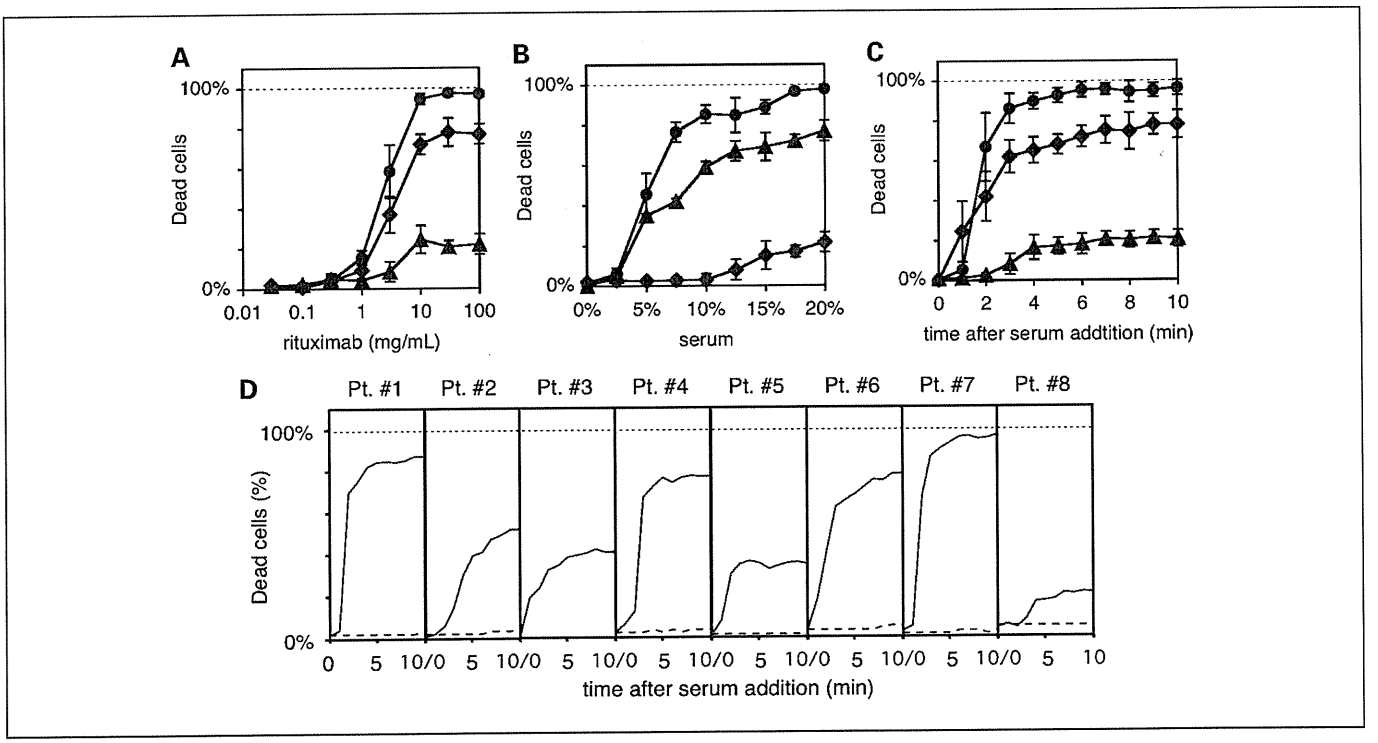

Fig. 2. Rituximab-mediated CDC assays on Burkitt's lymphoma cell lines and primary lymphoma cells. *A*, relationship between the rituximab concentrations and CDC-mediated cell killing in the presence of a final concentration of 20% human serum. Proportions of dead cells were counted and plotted against the rituximab concentrations. Circles, Ramos; diamonds, Raji, triangles, Daudi in *A, B* and *C. B*, relationship between the serum concentration and CDC-mediated cell killing in the presence of 10 μg/mL of rituximab. Proportions of dead cells were counted and plotted against the serum concentrations. *C*, time course of CDC-mediated cell killing in the presence of 10 μg/mL of rituximab and a final concentration of 20% human serum. Proportions of dead cells were counted and plotted against the time after serum addition. *D*, time course of CDC-mediated cell killing in lymphoma cells derived from biopsy of eight patients. Assay was done in the presence of 10 μg/mL of rituximab and at a final concentration of 20% human serum. All experiments were done in triplicate. Points, mean; bars, SD.

treatment was discontinued for reasons other than disease progression, for example, changing hospitals or developing severe (greater than grade 3/4) adverse events (four cases of DLBCL and four cases of FL).

Rituximab-containing chemotherapies. Thirty-three patients diagnosed with DLBCL and 30 patients with FL received cyclophosphamide, doxorubicin, vincristine, and prednisone (CHOP)–like chemotherapy plus rituximab; 7 patients with DLBCL and 7 with FL received a salvage chemotherapy plus rituximab. The salvage chemotherapy included ifosfamide, carboplatin, and etoposide (ICE) and dexamethasone, cytarabine, and cisplatin (DHAP). Both therapies included rituximab administration at a dose of 375 mg/m^2 i.v. at 1-week intervals of eight cycles. CHOP-like chemotherapy included all regimens with at least standard doses of doxorubicin (50 mg/m^2 i.v., day 1), cyclophosphamide (750 mg/m^2 i.v., day 1), vincristine [1.4 mg/m^2 i.v. (maximum 2 mg), day 1], and prednisone (60 mg/m^2 orally, days 1-5) administered in 3-week cycles.

Measurement of CDC susceptibility of patient-origin lymphoma cells. CD19-positive cells were purified as described in Materials and Methods. The purified cells were mixed with rituximab and human serum on the stage of a confocal microscope, and the CDC susceptibility index was calculated. The CDC susceptibility analysis was carried out by persons unable to access information about diagnosis results or treatment response. Characteristics of CDC susceptibility according to subtype of lymphoma are shown in Fig. 3A. In DLBCL and FL, the CDC susceptibility index had a remarkably wide distribution, from nearly 0% to 100%; means were 54% and 64%, respectively. A comparison with the cases other than B-cell non-Hodgkin's lymphoma showed no significant difference in mean CDC susceptibility; however, it should be noted that relatively low susceptibility cases were included in DLBCL

Table 1. Patient characteristics

Characteristics	DLBCL, *n* = 51	FL, *n* = 45
	n (%)	*n* (%)
Gender		
Female	21 (41)	25 (56)
Male	30 (59)	20 (44)
Age (y)		
<60	14 (27)	23 (51)
≥60	37 (73)	22 (49)
State of disease		
Primary	37 (73)	36 (80)
Relapse	14 (27)	9 (20)
IPI		
Low	31 (61)	20 (44)
Low-intermediate	4 (8)	11 (24)
High-intermediate	8 (16)	11 (24)
High	8 (16)	3 (7)
Treatment		
R-CHOP like	33 (65)	30 (67)
R-ICE	5 (10)	7 (16)
R-DHAP	2 (4)	0 (0)
Without R*	11 (20)	8 (18)

*Chemotherapy regimen without rituximab

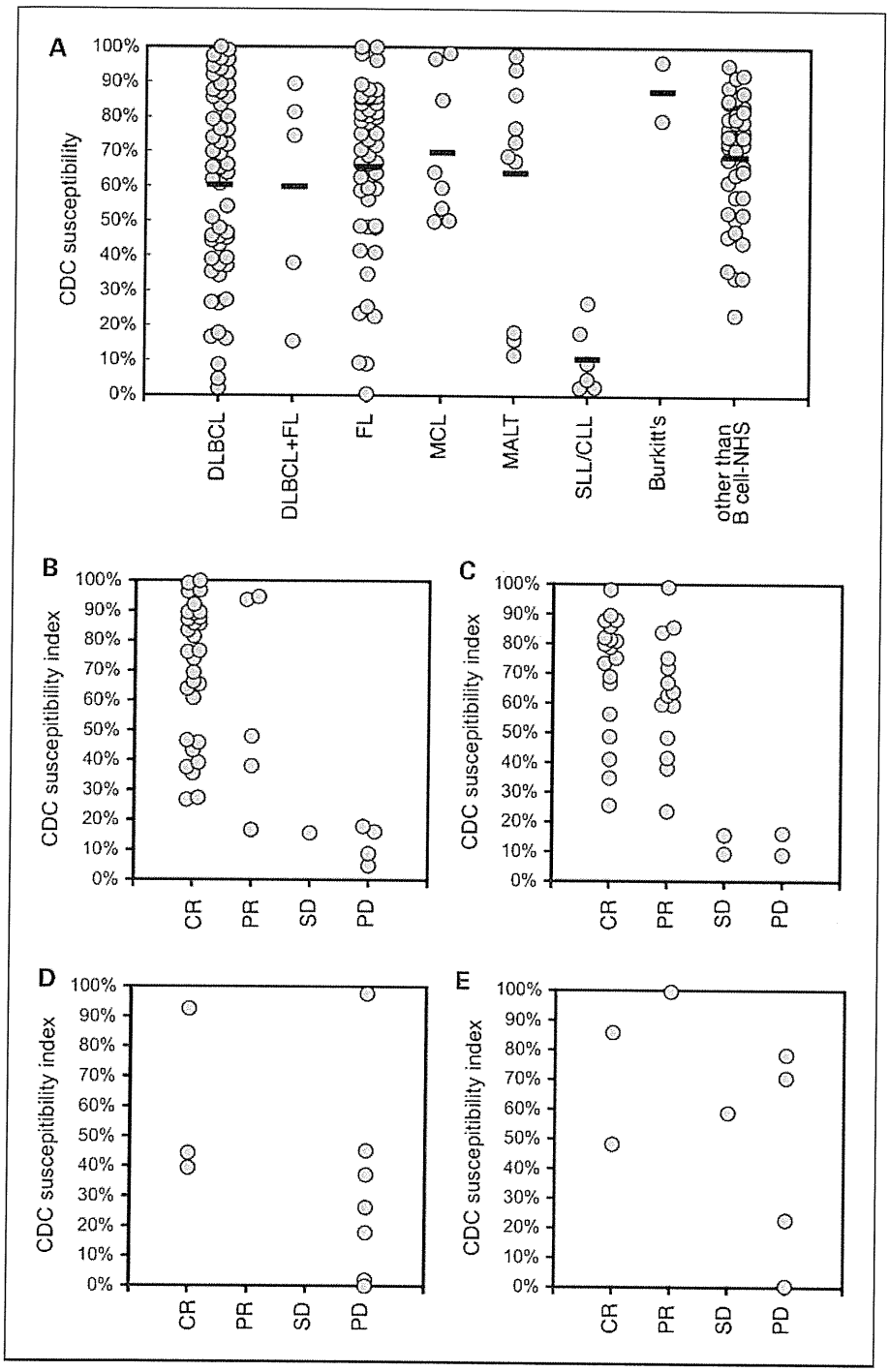

Fig. 3. Profiles of CDC susceptibility index. *A*, a total of 234 cases analyzed for CDC susceptibility were classified in eight categories of disease subtypes. The CDC susceptibility index of each case was plotted. Bar, mean. *B* to *E*, relationship between CDC susceptibility index of lymphoma cells obtained from patients with DLBCL (*B* and *D*) and FL (*C* and *E*) and clinical response of rituximab-containing chemotherapy. Lymphoma cells derived from 40 patients with DLBCL (*B*) and 37 patients with FL (*C*) who received the R+chemotherapy regimen were examined for CDC susceptibility and plotted against prognosis. Similarly, we examined lymphoma cells derived from 10 patients with DLBCL (*D*) and 8 patients with FL (*F*) who received chemotherapy without rituximab.

and FL cases. In mucosa-associated lymphoid tissue and Burkitt's lymphoma, the CDC susceptibility index of all cases we evaluated was >50%, and the means were 69% and 87%, respectively. In contrast, in chronic lymphocytic leukemia/small lymphocytic lymphoma, all cases were <29% with a mean index of 12%. In comparison with a non–B-cell lymphoma case, statistical significant difference was found only in chronic lymphocytic leukemia/small lymphocytic lymphoma cases ($P < 0.001$).

Relationships between CDC susceptibility and response to rituximab-containing chemotherapy. To clarify the association between CDC susceptibility and response to rituximab-containing combination chemotherapy, we did a correlation analysis for DLBCL and FL patients who had undergone CDC susceptibility analysis between January 2005 and December 2007. As for the DLBCL cases that received rituximab combination chemotherapy, 35 patients (87.5%) with complete response (CR) or partial response (PR) were judged effective, whereas 5 patients (12.5%) with stable disease (SD) or progressive disease (PD) were judged not effective. Similarly, for FL cases, 33 patients (89.2%) with CR or PR were judged effective, whereas 4 patients (10.8%) with SD or PD were judged not effective.

To assess the independent contribution of CDC susceptibility to the prediction of clinical response, multiple logistic

regression analysis was done. In the model, we used chemotherapeutic category (induction/salvage) and the International Prognostic Index (IPI) grade as confounding variables. The preceding univariate analysis showed that all these variables were significantly associated with the clinical response ($P < 0.001$, $P = 0.0338$, and $P = 0.0346$ for CDC, IPI, and chemotherapeutic category, respectively). Multiple stepwise logistic regression analysis showed that CDC susceptibility was an independent predictor of clinical response ($P < 0.001$), chemotherapeutic category was also another independent predictor ($P = 0.0473$); on the other hand, the IPI index was not considered to be an independent predictor in this multivariate model.

As CDC susceptibility was reported to be influenced by the target antigen expression levels (14), we then analyzed the relation between rituximab-induced CDC and cell surface CD20 expression levels, and compared their predictive ability. Analysis using Pearson's correlation coefficient indicated a statistically significant correlation between the CDC susceptibility index and CD20 expression level in lymphoma cells derived from patients with both FL and DLBCL (Supplemental Fig. S1; $r = 0.519$, $P < 0.01$, and $r = 0.592$, $P < 0.01$, respectively). ROC curves for both the CDC susceptibility index and CD20 expression levels to distinguish effective (CR + PR) versus noneffective (SD + PD) were produced. The area under the ROC curve for the CDC susceptibility index was significantly larger than that for the CD20 expression level (0.998; 95% confidence interval, 0.992-1.000; and 0.777; 95% confidence interval, 0.578-0.976, respectively; $P = 0.005$), indicating that the CDC susceptibility index was a more powerful discriminator of patients' response than CD20 antigen expression (Fig. 4, *top*).

The ROC curve analysis was further used to calculate the optimal cutoff value of CDC susceptibility for discriminating clinical response. A CDC susceptibility value of 18%, which provided the highest sensitivity and specificity, was selected to categorize lymphoma as high or low CDC susceptibility (Fig. 4, *bottom*). Using this cutoff value, we estimated the prognostic reliability of the CDC susceptibility index in rituximab combination chemotherapy. For DLBCL treated with R-CHOP–like therapy, the response rates were significantly higher in the cases with high CDC susceptibility (96.8% effective) than in those with lower susceptibility (0%; $P < 0.001$; two-sided Fisher's exact test). In addition, in the all-rituximab combination chemotherapy including R-salvage chemotherapy, the cases with high CDC susceptibility exhibited significantly higher response rates (97.2%) than those with a lower CDC index (0%; $P < 0.001$, two-sided Fisher's exact test). Similarly, even in FL, the CDC index showed statistically significant associations with therapy response to both R-CHOP–like therapy and all rituximab combination chemotherapies ($P = 0.0023$ and $P < 0.001$, respectively).

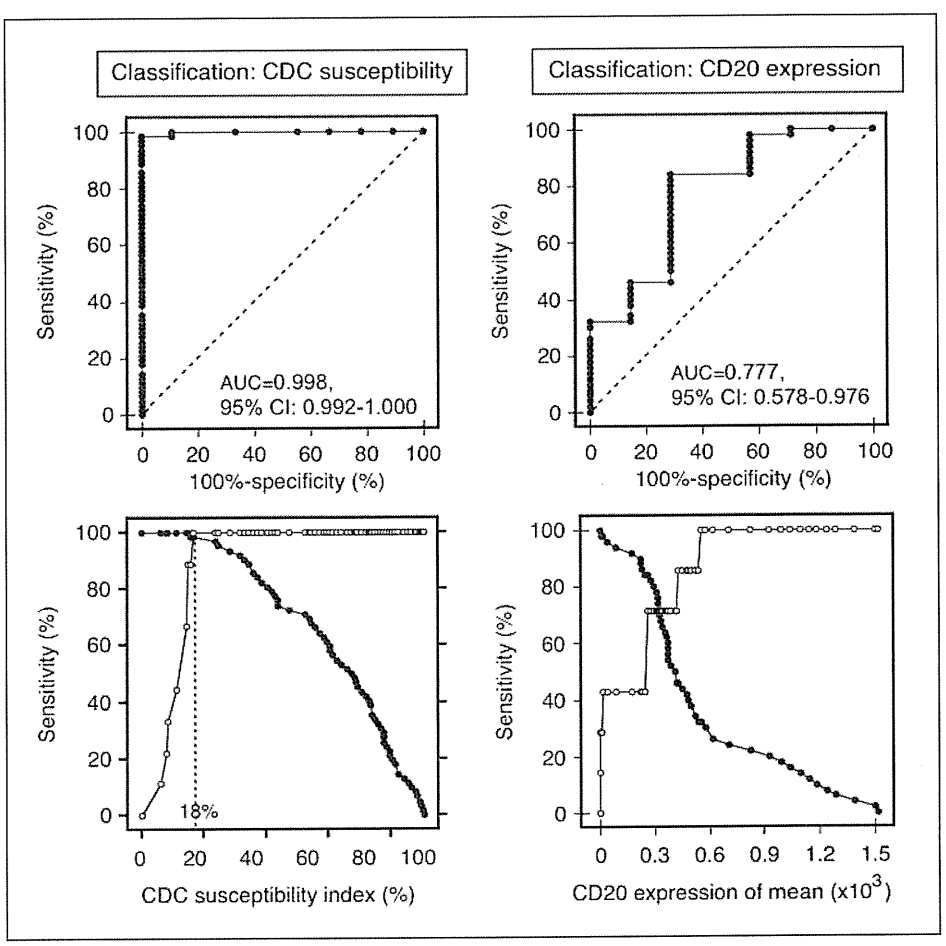

Fig. 4. Comparative analyses between CDC susceptibility and CD20 expression level. ROC curve analysis was done for comparison of predictive power of CDC susceptibility and antigen expression and for optimized threshold value determination. The analyses were conducted on all patients with DLBCL and FL who received the R+chemotherapy regimen, and ROC curves classified by CDC susceptibility index and CD20 expression level were generated (*top*). The areas under the ROC curve (AUC) summarizing the inherent capacity of parameters to discriminate a responder from a nonresponder were calculated. The optimal cutoff value that provides a trade-off between sensitivity (true positives; *solid circles*) and specificity (true negatives; *open circles*) was determined to be 18% for CDC susceptibility from the plot of sensitivity and specificity versus criterion value (*bottom*).

Discussion

Previous studies have suggested that several mechanisms might be involved in the therapeutic efficacy of rituximab, including ADCC (8-10), CDC (4, 11), and the induction of growth arrest or apoptosis (6, 15, 16). Both clinical (17, 18) and experimental (19) studies have offered evidence that ADCC plays an important role. On the other hand, the role of complements in rituximab treatment has been suggested by several preclinical studies. A study using cynomolgus monkeys showed that the ability to deplete CD20-positive cells was almost completely lost when IgG_4, which lacks complement-binding ability, was used in place of IgG_1 (20). In addition, the eradication of syngeneic murine EL4 tumor cells expressing human CD20 by rituximab is dependent on C1q, the first component of the classic pathway, and is independent of natural killer cells (21). Similarly, complement depletion using cobra venom factor markedly reduced the efficacy of rituximab in several lymphoma xenograft models (4). As for clinical evidence, the contribution of CDC to rituximab treatment was indirectly supported by several clinical observations. To give some instances, complement is consumed during rituximab treatment; in some cases, only CD59-positive cells having complement resistance remained after long-term rituximab treatment (11, 22). Thus, several animal models and clinical phenomena suggest the role of complement in rituximab treatment, but no strong, direct evidence of the clinical significance of CDC has yet been shown. It should also be noted that some findings are controversial. Weng and Levy have investigated *in vitro* CDC susceptibility, the expression of CD20, and complement inhibitors CD46, CD55, and CD59 on cryopreserved biopsy specimens from patients with FL, concluding that neither of these variables correlates with the reactivity of rituximab treatment (23).

In the present study, we established a rapid assay method for CDC analysis. Our assay system made it possible to perform an assay with only 40,000 lymphoma cells. In addition, it eliminated the lag-time between incubation and analysis that was unavoidable in other analyses such as flow cytometry methods. These features have contributed highly reproducible multiple measurements, even when only a tiny biopsy specimen could be obtained. Using this system, we evaluated the CDC susceptibility of cells derived from lymphoma patients within 6 hours after the biopsy and analyzed the relationship to clinical response. We succeeded in eliminating most of the influence of effector cells by removing CD19-negative cells from the assay specimen, suggesting that net CDC susceptibility could be estimated. Analysis results on FL and DLBCL suggested a strong correlation between CDC susceptibility and the clinical response to rituximab-containing chemotherapy. This result is inconsistent with the report of Weng and Levy. We believe that the inconsistency was, in part, caused by the method of evaluating CDC susceptibility. Our evaluation method assesses the intrinsic characteristics of the tumor cells by analyzing without cryopreservation after

Table 2. Clinical characteristics in relation to CDC susceptibility in patients with DLBCL and FL

Treatment	CDC susceptibility	Responder	Nonresponder	*P**
DLBCL				
R-CHOP like				
	CDC > 18%	30	0	$P = 0.00067$
	CDC < 18%	1	3	
R+salvage				
	CDC > 18%	5	0	$P = 0.048$
	CDC < 18%	0	2	
R+chemotherapy†				
	CDC > 18%	35	0	$P = 8.0 \times 10^{-6}$
	CDC < 18%	1	5	
Without R‡				
	CDC > 18%	3	4	$P = 0.48$
	CDC < 18%	0	3	
FL				
R-CHOP like				
	CDC > 18%	28	0	$P = 0.0023$
	CDC < 18%	0	2	
R+salvage				
	CDC > 18%	5	0	$P = 0.047$
	CDC < 18%	0	2	
R+chemotherapy†				
	CDC > 18%	33	0	$P = 1.5 \times 10^{-5}$
	CDC < 18%	0	4	
Without R‡				
	CDC > 18%	3	4	$P = 1$
	CDC < 18%	0	1	

*P values were obtained from two-tailed Fisher's exact tests.
†Chemotherapy plus rituximab including R-CHOP–like and R+salvage chemotherapy.
‡Chemotherapy regimen without rituximab.

biopsy and by optimizing assay conditions. Indeed, for some lymphoma cells derived from patients, different results in the CDC susceptibility were observed when the measurement was taken after freeze-thawing versus just after collection (data not shown).

The heterogeneity of the patient backgrounds and of the type of treatment made the data difficult to interpret. Therefore, we did a multivariate analysis to access the independence of CDC susceptibility from the patient background, including the IPI grade and the type of treatment, and found that CDC was a probable independent predictor for effectiveness. In our analysis, the IPI has a significant correlation with clinical response in univariate logistic analysis. However, in multivariate analysis, the IPI did not remain as an independent predictor, perhaps because the data included the salvage therapy. These results suggested that the CDC susceptibility index might be useful in predicting clinical response in both the induction and salvage chemotherapy containing rituximab. In addition, even by being limited to patients who received R-CHOP–like treatment as a first-line chemotherapy, significant correlation was found between CDC and clinical response in both FL and DLBCL (Table 2).

Although a significant correlation between CDC susceptibility index and the cell surface CD20 expression was also found in our analysis, the area under the ROC curve analysis revealed that the CDC susceptibility index was a more powerful discriminator of patients' response than CD20 antigen expression. In the responsive group, the CD20 expression had a wide distribution, including considerably low values (data not shown). These results indicate that cases that will get good therapeutic response in spite of low CD20 expression can be distinguished by CDC susceptibility.

To date, relationships between each mechanism of action, such as ADCC and CDC, have not been clarified completely in the clinical efficacy of therapeutic antibodies. A more detailed mechanism of action in rituximab-containing chemotherapy should be analyzed by evaluating the mutual action of CDC and ADCC. To further understand the relative clinical contribution of both effector mechanisms, we are currently developing an imaging-based reproducible ADCC evaluation system, and we plan to investigate the mutual relationship of ADCC and CDC, as well as the relationship between CDC/ADCC and long-term prognosis such as overall survival or relapse-free survival. These investigations will give us critical information about the exact therapeutic functions of these mechanisms.

The CDC susceptibility distinguished between responsive and refractory groups of rituximab-containing chemotherapy; however, it does not seem to be useful in more detailed classifications, such as complete response or partial response. In addition, the relation to clinical prognosis such as the duration of disease-free survival or overall survival is currently uncertain. In spite of these limitations, our analysis system provides a novel approach to predicting which patients will receive little benefit even if rituximab combination chemotherapy is done. Recently, antibody drugs using different mechanisms for B-cell non-Hodgkin's lymphoma have become increasingly available. Accordingly, it is expected that the prediction of the effects of therapeutic antibodies before the start of therapy will become more and more important in the post-rituximab era, leading to early implementation of optimal therapies, improving clinical outcomes.

In conclusion, we have shown that live cell–imaging is quite useful in improving CDC evaluation methods. The advantages of imaging-based procedures include needing only a minimal amount of specimen as well as rapidity and traceability. All of these features are advantageous to the analysis of clinical specimens. Thus, live cell–imaging may lead to greatly improved clinical evaluations.

Disclosure of Potential Conflicts of Interest

K. Hatake, commercial research support, honoraria, Chugai Pharmaceutical Co., Ltd.

Acknowledgments

We thank Sayuri Minowa and Harumi Shibata for their assistance in specimen preparation from lymph node biopsies; Chie Watanabe for help with the statistics; and Dr. Dovie Wylie of On-site English, Inc. (Palo Alto, CA) for English editing assistance.

References

1. Golay J, Zaffaroni L, Vaccari T, et al. Biologic response of B lymphoma cells to anti-CD20 monoclonal antibody rituximab *in vitro*: CD55 and CD59 regulate complement-mediated cell lysis. Blood 2000;95:3900–8.
2. Fischer L, Penack O, Gentilini C, et al. The anti-lymphoma effect of antibody-mediated immunotherapy is based on an increased degranulation of peripheral blood natural killer (NK) cells. Exp Hematol 2006;34:753–9.
3. Coiffier B. Monoclonal antibodies combined to chemotherapy for the treatment of patients with lymphoma. Blood Rev 2003;17:25–31.
4. Cragg MS, Glennie MJ. Antibody specificity controls *in vivo* effector mechanisms of anti-CD20 reagents. Blood 2004;103:2738–43.
5. Zhang N, Khawli LA, Hu P, Epstein AL. Generation of rituximab polymer may cause hyper-cross-linking-induced apoptosis in non-Hodgkin's lymphomas. Clin Cancer Res 2005; 11:5971–80.
6. Pedersen IM, Buhl AM, Klausen P, Geisler CH, Jurlander J. The chimeric anti-CD20 antibody rituximab induces apoptosis in B-cell chronic lymphocytic leukemia cells through a p38 mitogen activated protein-kinase-dependent mechanism. Blood 2002;99:1314–9.
7. Hatjiharissi E, Xu L, Santos DD, et al. Increased natural killer cell expression of CD16, augmented binding and ADCC activity to rituximab among individuals expressing the Fc{γ}RIIIa-158 V/V and V/F polymorphism. Blood 2007;110:2561–4.
8. Treon SP, Hansen M, Branagan AR, et al. Polymorphisms in FcγRIIIA (CD16) receptor expression are associated with clinical response to rituximab in Waldenstrom's macroglobulinemia. J Clin Oncol 2005;23:474–81.
9. Dall'Ozzo S, Tartas S, Paintaud G, et al. Rituximab-dependent cytotoxicity by natural killer cells: influence of FCGR3A polymorphism on the concentration-effect relationship. Cancer Res 2004;64:4664–9.
10. Cartron G, Dacheux L, Salles G, et al. Therapeutic activity of humanized anti-CD20 monoclonal antibody and polymorphism in IgG Fc receptor FcγRIIIa gene. Blood 2002;99:754–8.
11. Bannerji R, Kitada S, Flinn IW, et al. Apoptotic-regulatory and complement-protecting protein expression in chronic lymphocytic leukemia: relationship to *in vivo* rituximab resistance. J Clin Oncol 2003;21:1466–71.
12. Terui Y, Sakurai T, Mishima Y, et al. Blockade of bulky lymphoma-associated CD55 expression by RNA interference overcomes resistance to complement-dependent cytotoxicity with rituximab. Cancer Sci 2006;97:72–9.
13. Harjunpaa A, Junnikkala S, Meri S. Rituximab (anti-CD20) therapy of B-cell lymphomas: direct complement killing is superior to cellular effector mechanisms. Scand J Immunol 2000;51:634–41.
14. van Meerten T, van Rijn RS, Hol S, Hagenbeek A, Ebeling SB. Complement-induced cell death by rituximab depends on CD20 expression level and acts complementary to antibody-dependent cellular cytotoxicity. Clin Cancer Res 2006;12: 4027–35.
15. Byrd JC, Kitada S, Flinn IW, et al. The mechanism of tumor cell clearance by rituximab *in vivo* in patients with B-cell chronic lymphocytic leukemia: evidence of caspase activation and apoptosis induction. Blood 2002;99:1038–43.

16. Stel AJ, Ten Cate B, Jacobs S, et al. Fas receptor clustering and involvement of the death receptor pathway in rituximab-mediated apoptosis with concomitant sensitization of lymphoma B cells to fas-induced apoptosis. J Immunol 2007;178: 2287–95.
17. Weng WK, Levy R. Two immunoglobulin G fragment C receptor polymorphisms independently predict response to rituximab in patients with follicular lymphoma. J Clin Oncol 2003;21: 3940–7.
18. Anolik JH, Campbell D, Felgar RE, et al. The relationship of FcγRIIIa genotype to degree of B cell depletion by rituximab in the treatment of systemic lupus erythematosus. Arthritis Rheum 2003;48:455–9.
19. Clynes RA, Towers TL, Presta LG, Ravetch JV. Inhibitory Fc receptors modulate *in vivo* cytoxicity against tumor targets. Nat Med 2000;6:443–6.
20. Anderson DR, Grillo-Lopez A, Varns C, Chambers KS, Hanna N. Targeted anti-cancer therapy using rituximab, a chimaeric anti-CD20 antibody (IDEC-C2B8) in the treatment of non-Hodgkin's B-cell lymphoma. Biochem Soc Trans 1997;25:705–8.
21. Di Gaetano N, Cittera E, Nota R, et al. Complement activation determines the therapeutic activity of rituximab *in vivo*. J Immunol 2003;171: 1581–7.
22. van der Kolk LE, Grillo-Lopez AJ, Baars JW, Hack CE, van Oers MH. Complement activation plays a key role in the side-effects of rituximab treatment. Br J Haematol 2001;115:807–11.
23. Weng WK, Levy R. Expression of complement inhibitors CD46, CD55, and CD59 on tumor cells does not predict clinical outcome after rituximab treatment in follicular non-Hodgkin lymphoma. Blood 2001;98:1352–7.

The British Journal of Radiology, 82 (2009), e67–e71

CASE REPORT

Epstein–Barr virus-positive inflammatory pseudotumour and inflammatory pseudotumour-like follicular dendritic cell tumour

[1]S KIRYU, MD, PhD, [2]K TAKEUCHI, MD, PhD, [3]J SHIBAHARA, MD, PhD, [3]H UOZAKI, MD, PhD, [3]M FUKAYAMA, MD, PhD, [4]H TANAKA, MD, [1]E MAEDA, MD, [1]M AKAHANE, MD and [1]K OHTOMO, MD, PhD

[1]Department of Radiology, Graduate School and Faculty of Medicine, University of Tokyo, [2]Department of Pathology, Cancer Institute, Japanese Foundation for Cancer Research, [3]Department of Pathology, Graduate School and Faculty of Medicine, University of Tokyo and [4]Department of Diagnostic Radiology, Cancer Institute Hospital, Japanese Foundation for Cancer Research, Japan

ABSTRACT. Various splenic inflammatory pseudotumours are reported to be infected with Epstein–Barr virus (EBV), which is thought to be associated with the pathogenesis of the lesion. The term "inflammatory pseudotumour (IPT)-like follicular dendritic cell tumour", all cases of which are also EBV positive, has recently been proposed. Here, we describe the imaging findings of these splenic tumours and present the cases of an IPT-like follicular dendritic cell tumour and two EBV-positive inflammatory pseudotumours in two female patients and one male patient. These splenic lesions were found incidentally on pre-operative or post-operative screening or at medical check-up. CT performed on all three patients revealed low-density solitary masses in the spleen. MRI was performed on one patient; the solitary mass demonstrated isointensity on T_1 weighted images and low intensity on T_2 weighted images relative to the surrounding splenic parenchyma. Dynamic MRI study revealed that the mass did not enhance on the early phase but enhanced to the same degree as the surrounding splenic parenchyma on the delayed phase. The imaging findings are almost identical to those found in conventional IPT because the morphology is similar in both cases; however, attention should be paid to this new entity in the diagnosis of splenic lesions because of its neoplastic nature. Longer follow-up is also necessary for these patients compared with those with conventional IPT.

Received 26 June 2007
Revised 29 November 2007
Accepted 2 March 2008

DOI: 10.1259/bjr/66918927

Inflammatory pseudotumour (IPT) is a localized benign lesion — usually solitary — that is characterized by spindle cell proliferation with abundant inflammatory cells, mainly lymphocytes and plasma cells [1]. Several studies report splenic and hepatic IPTs to be associated with Epstein–Barr virus (EBV), which is found in 40.0–66.7% of splenic and hepatic IPTs; it is almost never detected at other sites [2–5].

Several cases of EBV-positive IPTs have recently been recognized to overlap with EBV-positive follicular dendritic cell (FDC) tumours. FDC tumours are a rare neoplasm and can arise in lymph nodes or extranodal sites [6–8]. Among FDC tumours, those in the liver and spleen demonstrate an IPT-like morphology and are infected with EBV [3, 9–11]. EBV infection is thought to be related to the neoplastic process of those lesions and the term "IPT-like FDC tumour" has recently been proposed. Therefore, EBV-positive IPTs require careful attention in the clinical course; this is in contrast to conventional IPTs, which are benign lesions.

Address correspondence to: Shigeru Kiryu, Department of Radiology, Graduate School of Medicine, University of Tokyo, 7-3-1 Hongo, Bunkyo-ku, Tokyo, 113-8655, Japan. E-mail: kiryu-tky@umin.ac.jp

The imaging findings of these lesions, especially those from MRI, have not been discussed fully. In this paper, we present three cases of splenic tumours, including EBV-positive IPTs and an IPT-like FDC tumour.

Case reports

Case 1

A 56-year-old woman underwent a medical check-up; a mass was revealed by ultrasound, but no abnormal laboratory data were observed. Contrast-enhanced CT confirmed a low-density, lobulated, well-circumscribed defined mass measuring 4 cm in the spleen (Figure 1). MRI was performed; the mass was isointense on T_1 weighted images using fast spin echo (repetition time/echo time (TR/TE) = 540/8 ms, echo train length = 3) and demonstrated low intensity on T_2 weighted images using fast spin echo (TR/TE = 4040/98 ms, echo length = 24) (Figure 2). A dynamic contrast-enhanced MRI study was performed using two-dimensional spoiled gradient-recalled acquisition in the steady state (TR/TE = 4.3/1.0 ms, flip angle = 15°) with fat saturation; the mass did not enhance on the early phase (30 s after

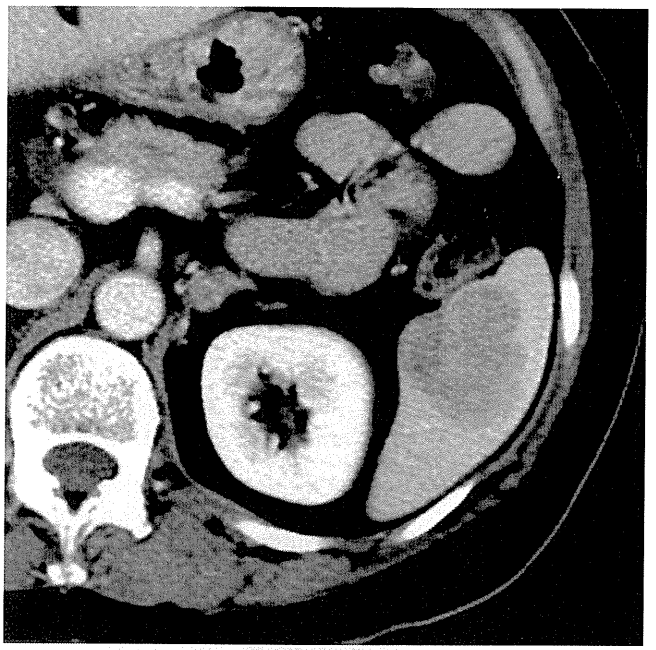

Figure 1. CT image of the abdomen of a 56-year-old woman (Case 1). Contrast-enhanced CT shows a low-density, lobulated, well-circumscribed defined mass.

administration of contrast agent) and enhanced to the same degree as the surrounding splenic parenchyma on the delayed phase (3 mins after administration of contrast agent). Splenectomy was performed, and the patient is alive and well at 2 years.

Case 2

A 60-year-old man was admitted to hospital with early gastric carcinoma. No abnormal laboratory data were observed. Contrast-enhanced CT was performed as a pre-operative examination; a low-density, round, well-defined mass measuring 2 cm was confirmed in the spleen (Figure 3). Splenectomy and gastrectomy were performed simultaneously, and the patient is alive and well at 4 years.

Case 3

A 78-year-old woman underwent contrast-enhanced CT for post-operative examination of breast carcinoma, which revealed a low-density, round, well-defined solitary mass measuring 3 cm in the spleen (Figure 4). The lesion was not found in pre-operative examinations. Splenic metastasis was suspected and splenectomy was performed. The patient is alive and well at 4 years.

Histopathological findings

The cut surfaces of the tumours revealed a well-circumscribed, milky white, solid mass without central necrosis (Figure 5).

The lesion was an admixture of lymphocytes, plasma cells and spindle cells, which is consistent with IPT (Figure 6a). The lymphocytes did not display atypical findings. *In situ* hybridization analysis for EBV-encoded RNA showed that spindle cells in the lesion were almost

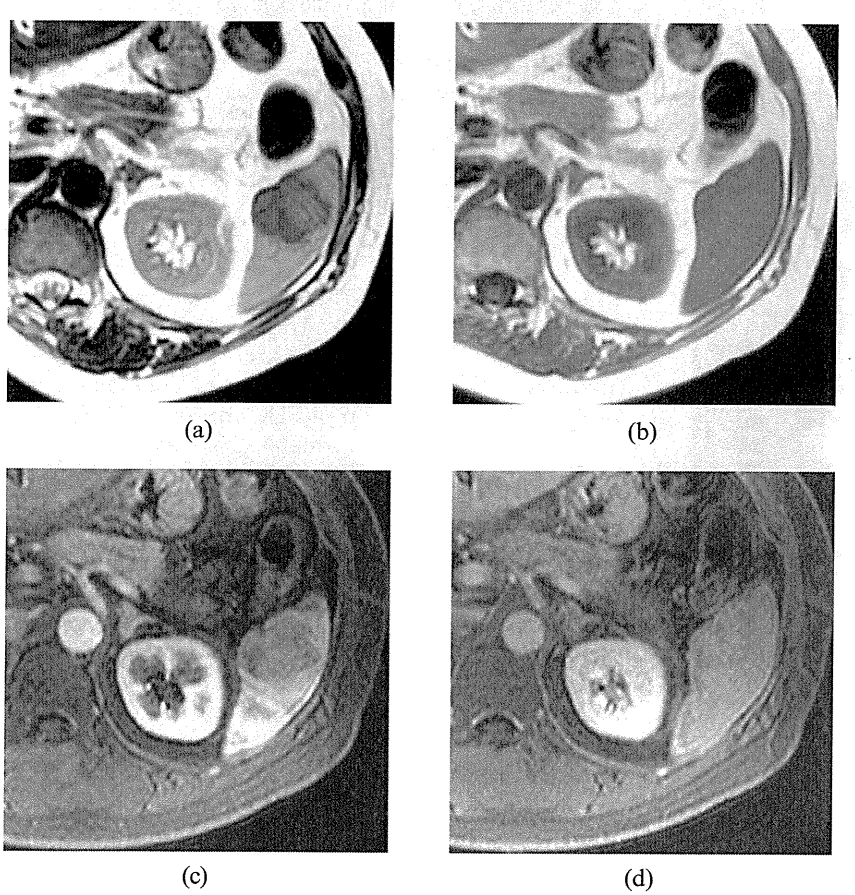

Figure 2. MRI images of the abdomen of a 56-year-old woman (Case 1). The mass displays low intensity on (a) the T_2 weighted image and isointensity on (b) the T_1 weighted image. On dynamic MRI, enhancement is not observed in (c) the early phase and delayed enhancement is shown on (d) the delayed phase.

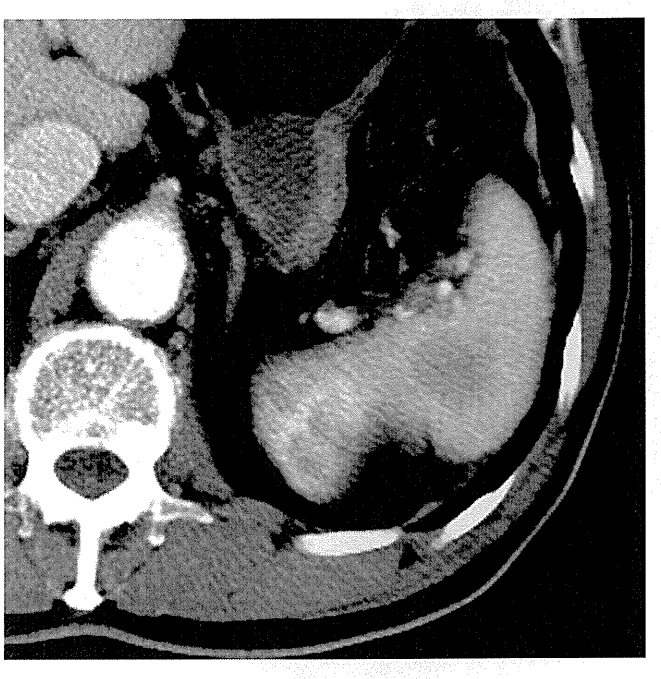

Figure 3. CT image of the abdomen of a 60-year-old man (Case 2). Contrast-enhanced CT reveals a low-density mass in the spleen.

exclusively EBV positive, whereas the cells in the surrounding splenic parenchyma were negative for EBV (Figure 6b). The spindle cells had pale or eosinophilic cytoplasm with indistinct cell borders; the nucleus was oval and pale with a centrally located small nucleolus.

In Case 1, most of the spindle cells were stained with FDC markers (CD21) (Figure 6c). The staining occurred in the cell membrane, highlighting the complex and interconnected dendritic cell processes. In Cases 2 and 3,

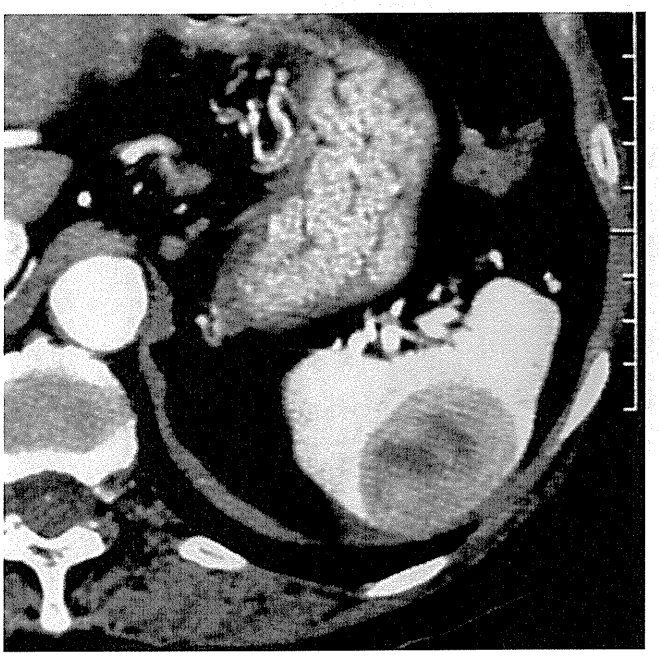

Figure 4. CT image of the abdomen of a 78-year-old woman (Case 3). Contrast-enhanced CT reveals a low-density mass in the spleen.

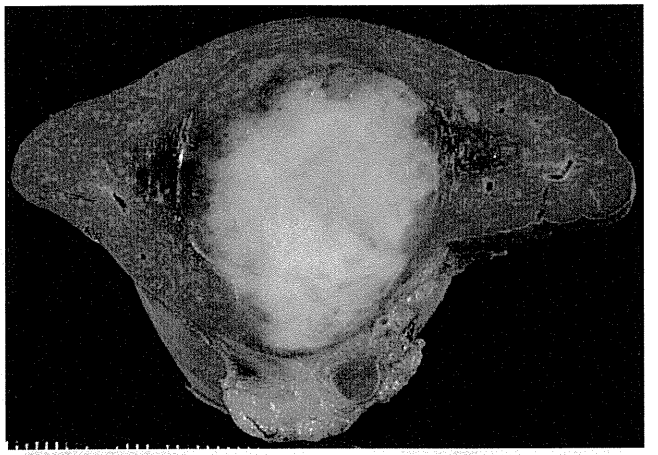

Figure 5. Surgical specimen of the spleen of a 56-year-old woman (Case 1). The cut surfaces reveal a well-circumscribed, milk-white coloured, solid mass without central necrosis.

spindle cells were not stained with FDC markers (CD21 for Case 2; CD21 and CD35 for Case 3).

Discussion

The existence of a primary neoplasm of lymph nodes showing features of FDC differentiation was reported by Monda et al [12] in 1986; since then, interest in FDC tumours has increased. FDC tumours can arise in lymph nodes or in extranodal sites, and extranodal intra-abdominal cases are known to pursue an aggressive clinical course [8, 13–15]. Among the reported cases of FDC tumours, several are associated with EBV; most of these cases involve the liver or spleen and demonstrate IPT-like morphology [3, 10]. In 2001, Cheuk et al [7] reported 11 EBV-positive FDC tumours with IPT-like morphology and proposed an entity — an IPT-like FDC tumour — as a distinctive variant of FDC tumour that differs in clinicopathological aspects from conventional FDC tumours.

Clinicopathological features and imaging findings of splenic EBV-positive IPTs and IPT-like FDC tumours are summarized in Table 1. There is a female predominance (male:female ratio = 5:9). The clinical presentation is non-specific and some patients are asymptomatic. Tumours ranged in size from 2 cm to 22 cm; seven cases confirmed the expression of FDC makers (IPT-like FDC tumour). No recurrence or metastasis was demonstrated for these IPT-like FDC tumours of the spleen, excluding five cases for which information was not available. On imaging, six cases demonstrated low-density lesions on plain or enhanced CT. The MRI findings are available for three cases; ours is the first to confirm the expression of FDC markers. The lesions are characterized by low intensity on T_2 weighted images and isointensity on T_1 weighted images. Delayed enhancement is observed on dynamic study. In previous reports, IPT was demonstrated on CT as an iso- or low-density mass on plain and enhanced phases [16, 17]. On MRI, IPT was characterized by its low intensity on T_2 weighted images, caused by massive fibrotic stroma, which is a characteristic histopathological finding of IPT [16, 18, 19]. The fibrotic stroma also causes the delayed enhancement on dynamic

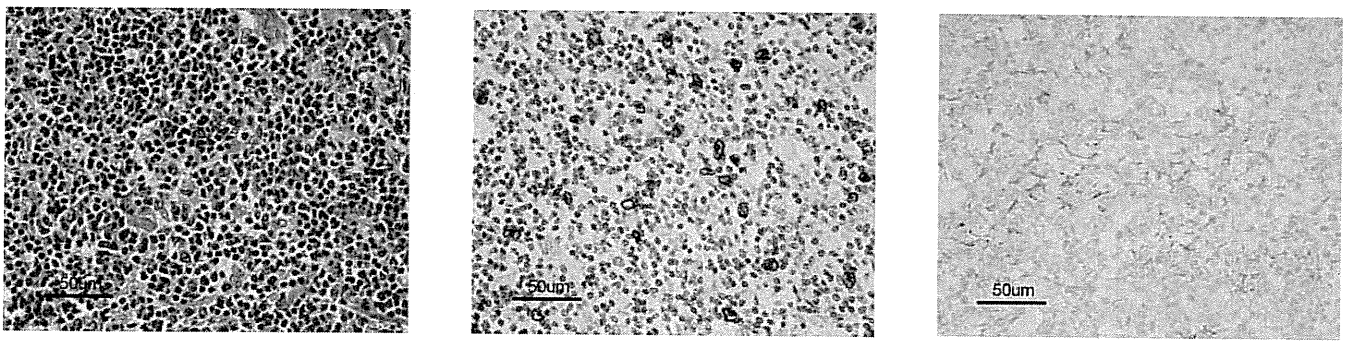

(a) (b) (c)

Figure 6. Histopathological tumour findings from a 56-year-old woman (Case 1). (a) Haematoxylin and eosin stain; (b) Epstein–Barr virus-encoded small RNA *in situ* hybridization; (c) immunostaining for a follicular dendritic cell marker (CD21).

study. Along with morphology that resembles IPT, the CT and MRI findings of the cases presented here are consistent with those of previous reports of IPT. The differential diagnosis includes tumours that are more common in the spleen, such as cavernous haemangioma, lymphangioma, metastasis, hamartoma and lymphoma. Cavernous haemangioma and lymphangioma usually show high intensity on T_2 weighted images [20, 21]. Although splenic hamartoma shows delayed enhancement, it tends to be of high intensity on T_2 weighted images [22]. Therefore, these lesions may be differentiated from EBV-positive IPTs and IPT-like FDC tumours on T_2 weighted images. To differentiate IPTs from common splenic malignant tumours such as metastasis and lymphoma is difficult, as the findings are the same as those of conventional IPTs. Hence, the prospective diagnosis of EBV-positive tumours is difficult.

EBV-positive IPT-expressing FDC markers and IPT-like FDC tumours are probably of the same disease entity, although more discussion is required to clarify their relationship. No clinicopathological or imaging-based differences have been recognized in the literature or in the present case series, except for the expression of "conventional" FDC markers. Thus, we believe that all of these EBV-positive tumours should be grouped under the same name, *e.g.* "splenic stromal tumour". In this scenario, EBV-positive IPTs without FDC markers might have lacked "conventional" FDC markers (CD21 and CD35) for an unknown reason. More reliable FDC marker(s) might serve to prove this scenario.

Table 1. Characteristics of patients described in the literature with IPT with EBV infection and IPT-like FDC tumours

Case	Sex/ age (years)	Presentation	Maximal diameter (cm)	FDC	CT	MRI[a]	Treatment; outcome
1	M/33	Anaemia and fatigue	NA	–	NA	NA	Splenectomy; NA
2	M/66	Epigastric pain	11.5	–	NA	NA	Splenectomy; NA
3	F/87	Incidental autopsy	1.5	–	NA	NA	Splenectomy; NA
4	M/70	Asymptomatic	5.5	+	NA	NA	Splenectomy; NA
5	F/63	Asymptomatic	5	NA	Low on enhanced	Iso/low, enhanced	Splenectomy; NA
6	F/58	Abdominal fullness and easy bruising	22	+	NA	NA	Splenectomy; alive and well at 4 months
7	F/39	Malaise, weight loss and fever	7.5	+	NA	NA	Splenectomy; alive at 2 months with persistent fever
8	F/61	Asymptomatic	3.5	+	NA	NA	Splenectomy; recent case
9	F/36	Nausea and insomnia	6.5	NA	NA	Iso/low, enhanced	Splenectomy; not available
10	F/77	Epigastralgia	11	+	Low on plain	NA	Splenectomy; alive and well at 3 years
11	M/54	Asymptomatic	12	+	Low on plain and enhanced	NA	Splenectomy; alive and well at 4 years
12	F/56	Asymptomatic	4	+	Low on enhanced	Iso/low, enhanced	Splenectomy; alive and well at 2 years
13	M/60	Asymptomatic	2	–	Low	NA	Splenectomy; alive and well at 4 years
14	F/78	Asymptomatic	2	–		NA	Splenectomy; alive and well at 4 years

Cases 1–4 were reported by Arber et al [3]; Case 5 was reported by Yamaguchi et al [2]; Cases 6–8 were reported by Cheuk et al [7]; Case 9 was reported by Oz Puyan et al [4]; Case 10 was reported by Horiguchi et al [9]; Case 11 was reported by Brittig et al [11]; and Cases 12–14 are current patients.

IPT, inflammatory pseudotumour; EBV, Epstein–Barr virus; FDC, follicular dendritic cell; NA, not available.

[a] T_1 weighted/T_2 weighted image.